PB85-128452

NIMBUS-7 SBUV (Solar Backscatter Ultraviolet) Observations of Solar UV Spectral Irradiance Variations Caused by Solar Rotation and Active-Region Evolution for the Period November 7, 1978-November 1, 1980

(U.S.) National Oceanic and Atmospheric Administration, Rockville, MD

Sep 84

NOAA Technical Memorandum ERL ARL-129

NIMBUS-7 SBUV OBSERVATIONS OF SOLAR UV SPECTRAL IRRADIANCE VARIATIONS CAUSED BY SOLAR ROTATION AND ACTIVE-REGION EVOLUTION FOR THE PERIOD NOVEMBER 7, 1978 - NOVEMBER 1, 1980

Donald F. Heath
Thomas P. Repoff
Richard F. Donnelly

Air Resources Laboratory
Rockville, Maryland
September 1984

noaa NATIONAL OCEANIC AND ATMOSPHERIC ADMINISTRATION / Environmental Research Laboratories

BIBLIOGRAPHIC INFORMATION

PB85-128452

NIMBUS-7 SBUV (Solar Backscatter Ultraviolet) Observations of Solar UV Spectral Irradiance Variations Caused by Solar Rotation and Active-Region Evolution for the Period November 7, 1978-November 1, 1980.

Sep 84

by D. F. Heath, T. P. Repoff, and R. F. Donnelly.

PERFORMER: National Oceanic and Atmospheric Administration, Rockville, MD. Air Resources Lab.
NOAA-TM-ERL-ARL-129

See also PB84-108166. Prepared in cooperation with National Aeronautics and Space Administration, Greenbelt, MD. Goddard Space Flight Center.

NIMBUS-7 SBUV observations of temporal variations of the solar UV spectral irradiance over several days to a few weeks in the 160-400 nm wavelength range are presented in detail for the period Nov. 7, 1978 to Nov. 1, 1980. Larger 28-day variations and a second episode of 13-day variations occurred during the second year of measurements. The thirteen day periodicity is not a harmonic of the 28-day periodicity. The 13-day periodicity dominates certain episodes of solar activity while others are dominated by 28-day periods accompanied by a weak 14-day harmonic. Techniques for removing noise and long-term trends are described. Time series analysis results are presented for the Si II lines near 182 nm, the Al I continuum in the 190 -205 nm range, the Mg I continuum in the 210 -250 nm range, the Mg II H & K lines at 280 nm, the Mg I line at 285 nm, and the Ca II K & H lines at 393 and 397 nm.

KEYWORDS: *Solar ultraviolet radiation, *Irradiance, *Solar spectrum.

Available from the National Technical Information Service, SPRINGFIELD, VA. 22161

PRICE CODE: PC A05/MF A01

NOAA Technical Memorandum ERL ARL-129

NIMBUS-7 SBUV OBSERVATIONS OF SOLAR UV SPECTRAL IRRADIANCE VARIATIONS CAUSED BY SOLAR ROTATION AND ACTIVE-REGION EVOLUTION FOR THE PERIOD NOVEMBER 7, 1978 - NOVEMBER 1, 1980

Donald F. Heath
Thomas P. Repoff
Richard F. Donnelly

Air Resources Laboratory
Rockville, Maryland
September 1984

UNITED STATES
DEPARTMENT OF COMMERCE

Malcolm Baldrige,
Secretary

NATIONAL OCEANIC AND
ATMOSPHERIC ADMINISTRATION

John V. Byrne,
Administrator

Environmental Research
Laboratories

Vernon E. Derr
Director

NOTICE

Mention of a commercial company or product does not constitute an endorsement by NOAA Environmental Research Laboratories. Use for publicity or advertising purposes of information from this publication concerning proprietary products or the tests of such products is not authorized.

This report extends the period of data studied in NOAA Technical Report ERL 424-ARL 7, "NIMBUS-7 SBUV Observations of Solar UV Spectral Irradiance Variations Caused by Solar Rotation and Active-Region Evolution for the Period November 7, 1978-October 26, 1979" (Heath et al., 1983). Where the earlier report covered one year, this report covers two years and includes much more sophisticated analysis techniques.

TABLE OF CONTENTS

NIMBUS-7 SBUV Observations of Solar UV Spectral Irradiance Variations Caused by Solar Rotation and Active-Region Evolution For the Period November 7, 1978 - November 1, 1980

Donald F. Heath[1], Thomas P. Repoff[2] and Richard F. Donnelly[2]

1. Laboratory for Planetary Atmospheres, NASA Goddard Space Flight Center, Greenbelt, Maryland 20771

2. Sun-Climate Office, Air Resources Laboratories, NOAA ERL, Boulder, Colorado 80303

ABSTRACT

NIMBUS-7 SBUV observations of temporal variations of the solar UV spectral irradiance over several days to a few weeks in the 160 - 400 nm wavelength range are presented in detail for the period Nov. 7, 1978 to Nov. 1, 1980. Larger 28-day variations and a second episode of 13-day variations occurred during the second year of measurements. The thirteen day periodicity is not a harmonic of the 28-day periodicity. The 13-day periodicity dominates certain episodes of solar activity while others are dominated by 28-day periods accompanied by a weak 14-day harmonic. Techniques for removing noise and long-term trends are described. Time series analysis results are presented for the Si II lines near 182 nm, the Al I continuum in the 190 - 205 nm range, the Mg I continuum in the 210 - 250 nm range, the Mg II H & K lines at 280nm, the Mg I line at 285 nm, and the Ca II K & H lines at 393 and 397 nm.

1. INTRODUCTION

This report describes the analysis of solar UV irradiance measurements in the 160 - 400 nm wavelength range from the Solar Backscatter Ultraviolet (SBUV) Experiment aboard the NIMBUS-7 satellite for the first two years of observations from November 7, 1978, through November 1, 1980. The 160 - 290 nm solar UV flux is important because of its effect on the stratosphere as a heat source and as the initiator of the photochemistry that produces important constituents like ozone. In Chapter 2, the short-term solar UV flux variations caused by solar rotation and active region evolution are described for the eight largest cases during the second year of NIMBUS-7 observations, which extends the similar results for the first year of observations given in

the first report in this series (Heath et al., 1983). Chapter 3 includes simple analysis of the relation of the aluminum continuum enhancements to the enhancements in the wavelength range of the magnesium continuum in the solar spectrum. The Al I continuum enhancements are very important for enhancing the photodissociation of O_2 to produce atomic oxygen in the stratosphere. The enhancements in the wavelength range of the magnesium continuum are important because they enhance the heating of the stratosphere.

Chapters 4 - 8 describe time series analyses that we are now applying to many solar flux measurements and solar indices, where journal papers on the physical interpretation of the analysis results will depend on this report as our main reference for the details of the analysis procedures. Chapter 4 describes the removal of noise and long-term trends in preparation for statistical studies of the short-term variations caused by solar rotation and active region evolution. Chapter 5 describes the autocorrelation analysis in the time domain and the power spectrum analysis in the frequency domain for the major lines and the Al I continuum in the solar UV spectrum. Comparison of the time-series characteristics at two different UV wavelengths is discussed in Chapter 6 with cross-correlation and cross-spectrum analyses. Complex demodulation analysis in Chapter 7 shows that the solar UV flux has some episodes with strong 28-day and weak 13-day periodicity and, conversely, other episodes with strong 13-day and weak 28-day periodicity. Chapter 8 describes planned future analyses and Chapter 9 summarizes our conclusions.

Heath et al. (1975) have described the Solar Backscatter Ultraviolet (SBUV) Experiment in detail. Briefly, the main goal of the experiment is to observe the global distribution of ozone as a function of altitude. A second result, the only one discussed here, is the measurement of the solar spectral irradiance in the 160 - 400nm range. The SBUV experiment is aboard the

NIMBUS-7 satellite, which flies a polar orbit. Usually, about three to four scans of the solar spectrum are recorded within about a five minute period each day, typically for three days in a row followed by no measurements on the fourth day. Starting on January 23, 1980, measurements were also made on the fourth days. On October 1, 1979, and after July 14, 1980, three to four wavelength scans were recorded for each orbit for about thirteen orbits per day, i. e. measurements were made during about five minute intervals separated by a little less than two hours throughout the day. Daily averages were used in this study to improve the signal to noise ratio.

The spectrometer bandpass is about 1.0 nm and the steps in wavelength are about .2 nm. The SBUV instrument includes a reference photodiode to calibrate in flight the gain of the photomultiplier tube. Corrections for degradation in the photomultiplier gain have been included in the data analyzed. Long-term degradation of the diffuser used in the solar irradiance measurements has been discovered and corrections are being developed but are not included in the data analyzed here. However, our analysis described in Chapter 4 was designed to minimize the effect of long-term instrumental drifts on this study of short-term solar UV flux variations.

2. EIGHT CASES OF SOLAR ULTRAVIOLET VARIATIONS

Figure 2.1 shows the time dependence of SBUV measurements for the first two years of NIMBUS-7 observations. Most of the long-term variations represented by the smooth background curve are of instrumental origin and do not represent real variations in the solar UV flux. The instrumental variations include degradation of the diffuser used to deflect the solar radiation into the spectrometer and an asymmetric semiannual variation. Starting in January, 1980, the solar observations were made every day rather than three out of four days; however, the instrument operating temperature was distinctly different on these "fourth days" because the rest of the experiments were not operated as they were on the other three out of four days. Consequently, these "fourth-day" measurements were consistently lower and cause the fourth-day noise evident in Figure 2.1. The removal of noise and long-term trends is discussed in Chapter 4. In the analysis in this chapter, their effect was reduced by considering individual solar rotation variations and deleting the "fourth-day" data.

Figure 2.1 shows the NIMBUS-7 observations of the major lines and continuum in the spectrum of short-term UV variations (Heath et al., 1983). The 181.6 - 182.2 nm band includes Al I continuum emission and two Si II emission lines. The 200 - 205 nm observations are at the head of the Al I absorption continuum in the solar spectrum. The 279.7 - 280.1 nm measurements are at the center of the Mg II H & K absorption line pair, the 285.1 - 285.3 range includes the solar Mg I absorption line, 393.3 - 393.7 nm includes the Ca II K absorption line and 396.9 to 397.1 nm includes the solar Ca II H absorption line. The Mg II observations show a larger percentage variation than the Ca II observations probably partly because Mg II is at much shorter wavelengths where the percentage flux variation for a given change in source

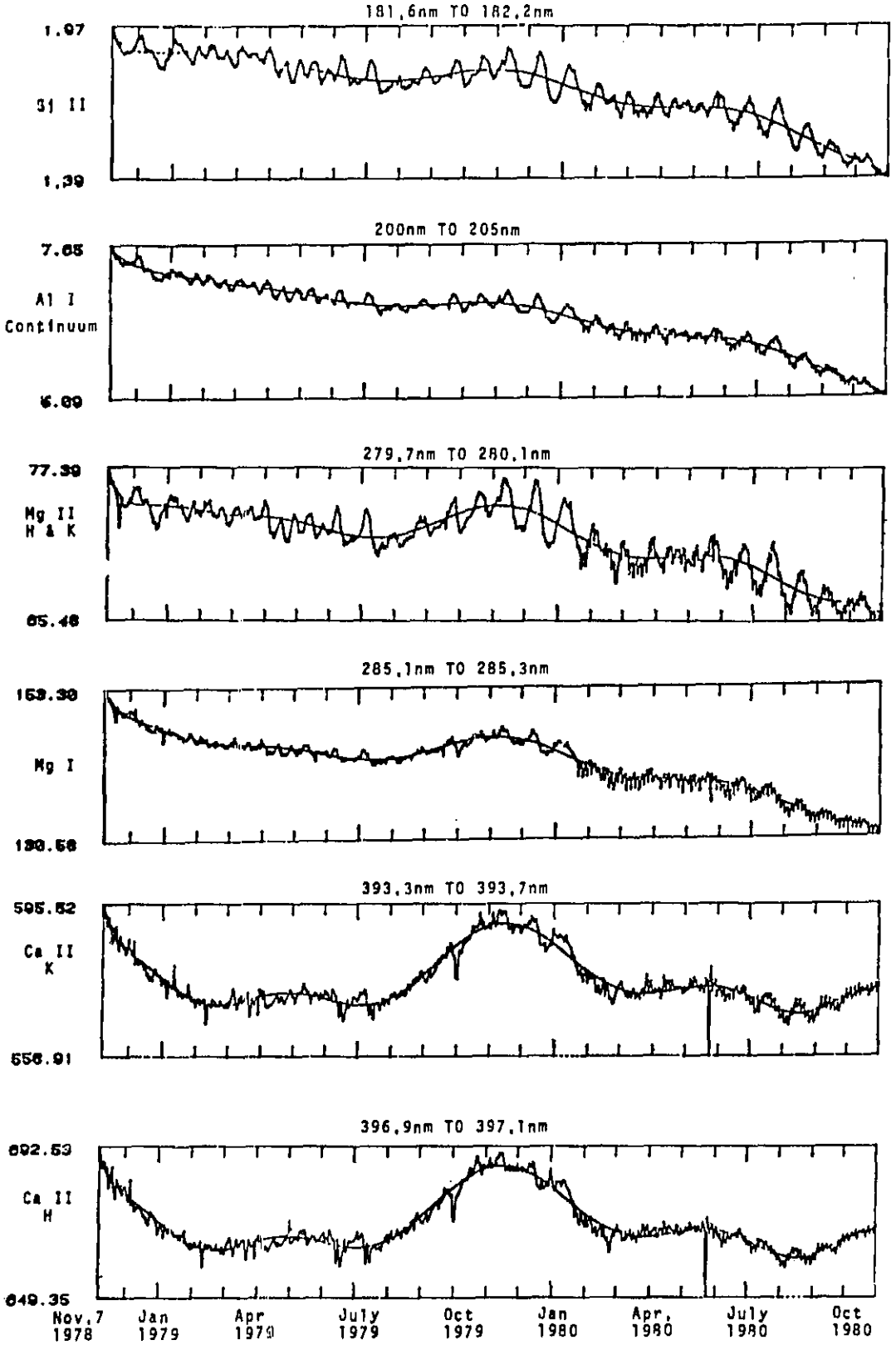

Figure 2.1 First two years of SBUV measurements of the solar flux from the NIMBUS-7 satellite. See the text and chapter 4 for a discussion of noise, long-term drifts and the smooth background curve.

temperature tends to be larger. The percentage variations of the Mg II line is also larger than that of the Ca II lines or the Mg I line partly because the former involves two chromospheric cores from the unresolved H & K lines while the two Ca II H & K lines are observed separately. The instrument bandpass is about 1 nm, which fits deeper into the Mg II absorption line pair than into the narrower Mg I absorption line. Consequently, the Mg II center-of-line measurements involve a larger portion of emission from the more highly varying chromosphere relative to the weakly varying photosphere than in the case of the Mg I line. Furthermore, the Mg I line oginates from lower in the solar atmosphere and does not have a strong chromospheric emission core like the Mg II line pair. Therefore, it is not surprising that the Mg I line exhibits smaller percentage variations than the Mg II line pair. It is more interesting that the Mg I line varies as much as it does with temporal shapes so similar to the Mg II line pair.

The strongest short-term variations shown in Figure 2.1 occur near the peak of solar cycle 21 in November and December 1979, and January 1980, and in June and July, 1980. The strong short-term variations have periods near 28 days (periodicity is analyzed in Chapters 5 - 7) and involve several intense plages at their peaks and even several moderate to weak intensity plages during their local minima. So larger short-term variations occurred during the second year of NIMBUS-7 observations than during the first year. Periods near thirteen days occurred from late January to June, 1979, and again during February - May, 1980. Note that the amplitude of these thirteen-day variations is smaller on average than for the variations with dominant periods near 28 days. This is caused by shallower valleys because the groups of plages that cause the peaks are not completely out of view at the times of the valleys. These cases of thirteen-day variations have been discussed by Donnelly et al., (1982, 1983, 1984).

The wavelength spectrum of the ratio of maximum to minimum UV flux of short-term UV temporal variations caused by the solar rotation of an inhomogeneous distribution of active regions was calculated for eight cases recorded during the second year of NIMBUS-7 observations from the formula

$$\text{Ratio} = 2\,\Phi(t = \text{peak})/[\Phi(t = \text{preceding min.}) + \Phi(t = \text{following min.})]. \quad (1)$$

The average of the preceding and following minima was used to reduce the errors caused by the long-term instrumental drifts evident in Figure 2.1. The ratios as a function of wavelength are given in Figures 2.2 - 2.9. The dates of the maximum and preceding and following minima are given in each figure.

In the first report of this series (Heath et al., 1983), similar results were presented for the 15 largest variations recorded in the first year of NIMBUS-7 observations. Those results involved the average of two to three days for each maxima or minima to reduce the effect of noise. The present eight cases are the largest in the second year of data and most of them are larger in amplitude than all the variations from the first year. Consequently, there was less need to use three-day time averages to reduce noise, and only one daily average was used for each minima and maxima. These eight cases involve data that were not detrended or edited for bad data as described in chapter 4, except the faulty "fourth-day" observations were not included.

The main features in Figures 2.2 - 2.9 are the solar Al I absorption edge and continuum at wavelengths below 210 nm and the Mg II H and K lines combined at 280 nm (unresolved with 1 nm bandpass). The combined Si II lines appear at 182 nm, a Mg I line at 285 nm, and the Ca II H and K lines at about 393 and 397nm, respectively. Numerous lines of Fe I, Fe II, Al I and Si I appear in the 210 - 277 nm range and possibly a continuum of Mg I below about 251 nm (see Heath et al., 1984). The results below 180 nm are quite noisy.

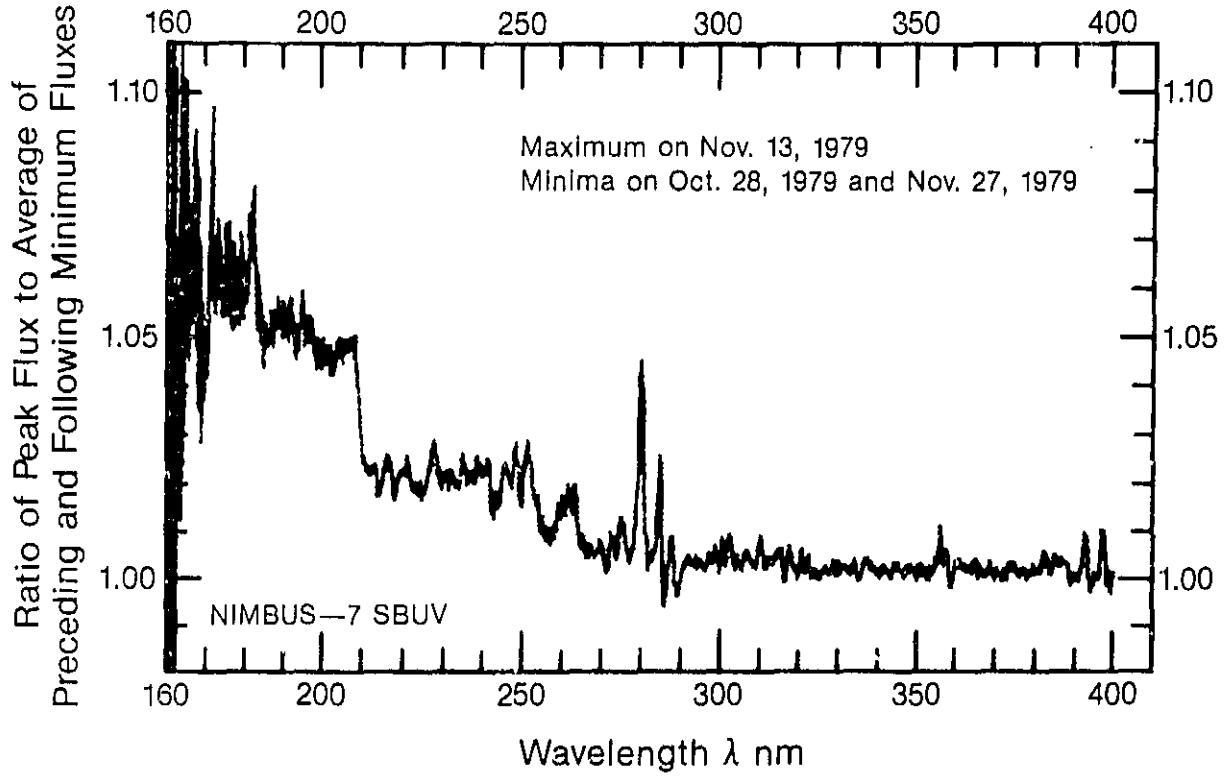

Figure 2.2 Spectrum of the Short-Term Variation that Peaked on Nov. 13, 1979.

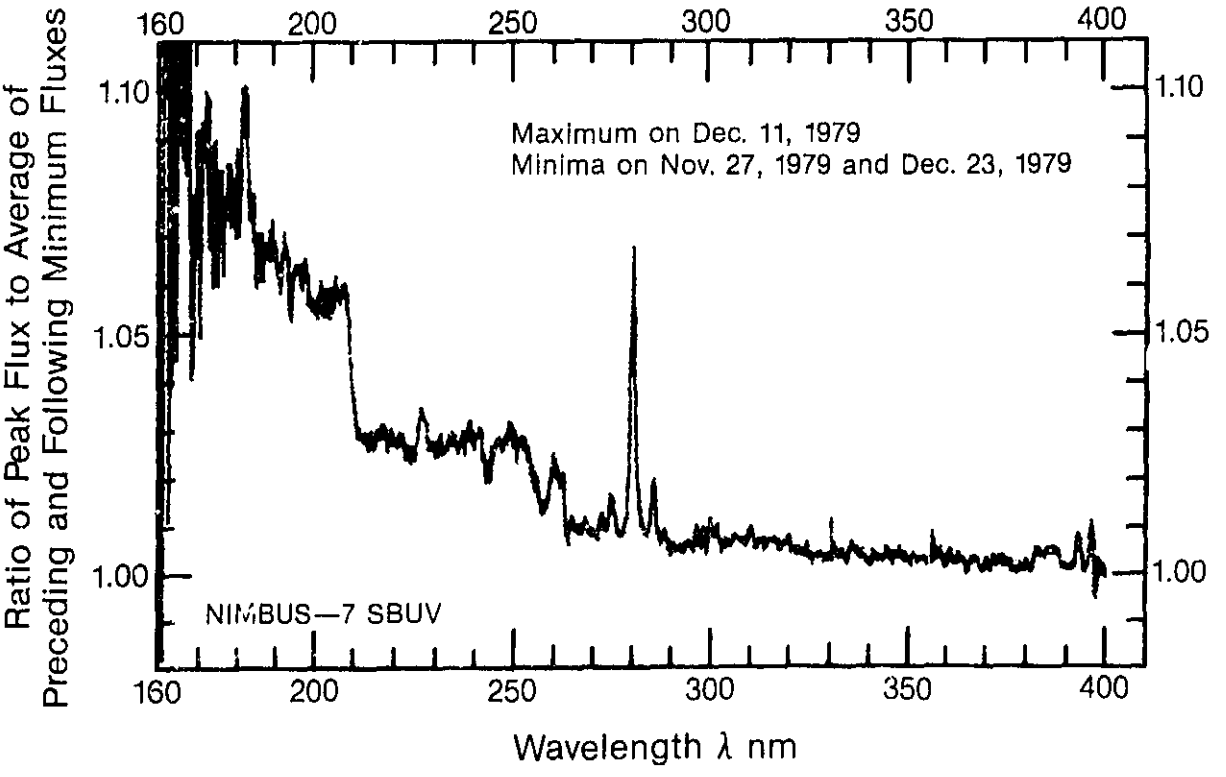

Figure 2.3 Spectrum of the Short-Term Variation That Peaked on Dec. 11, 1979.

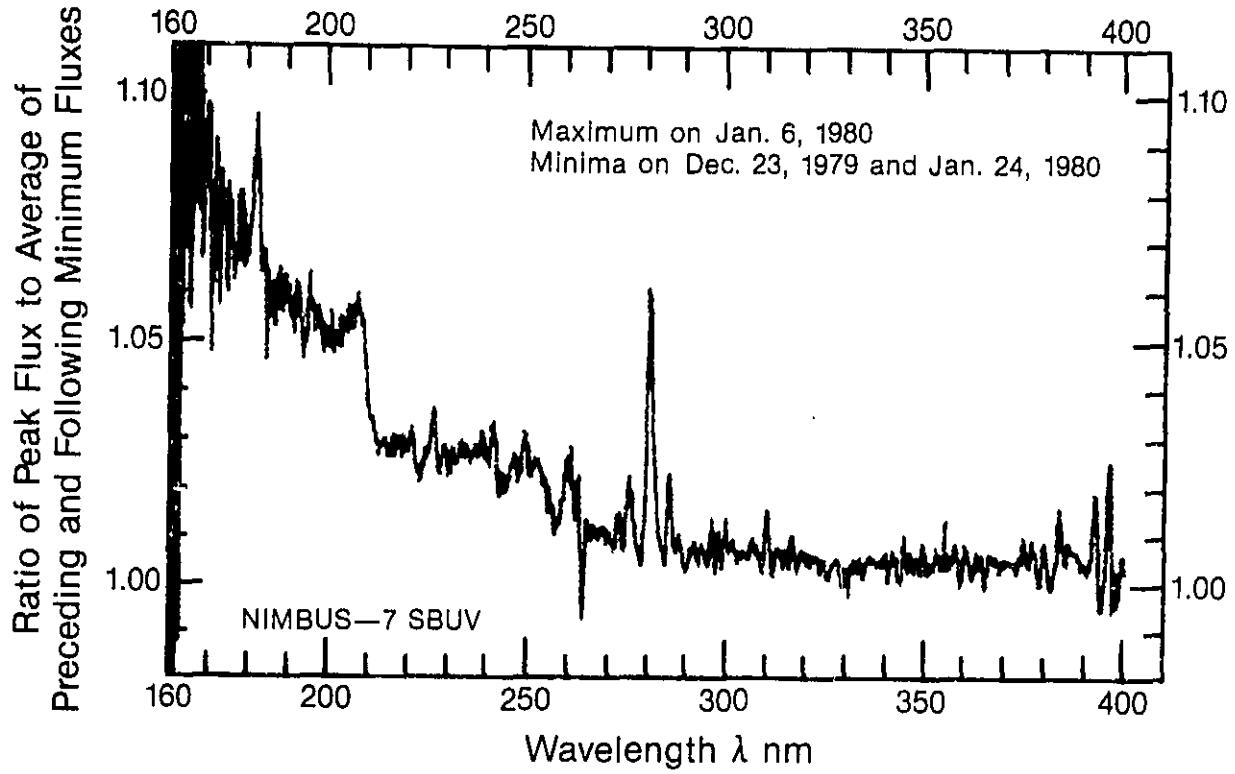

Figure 2.4 Spectrum of the Short-Term Variation that Peaked on Jan. 6, 1980.

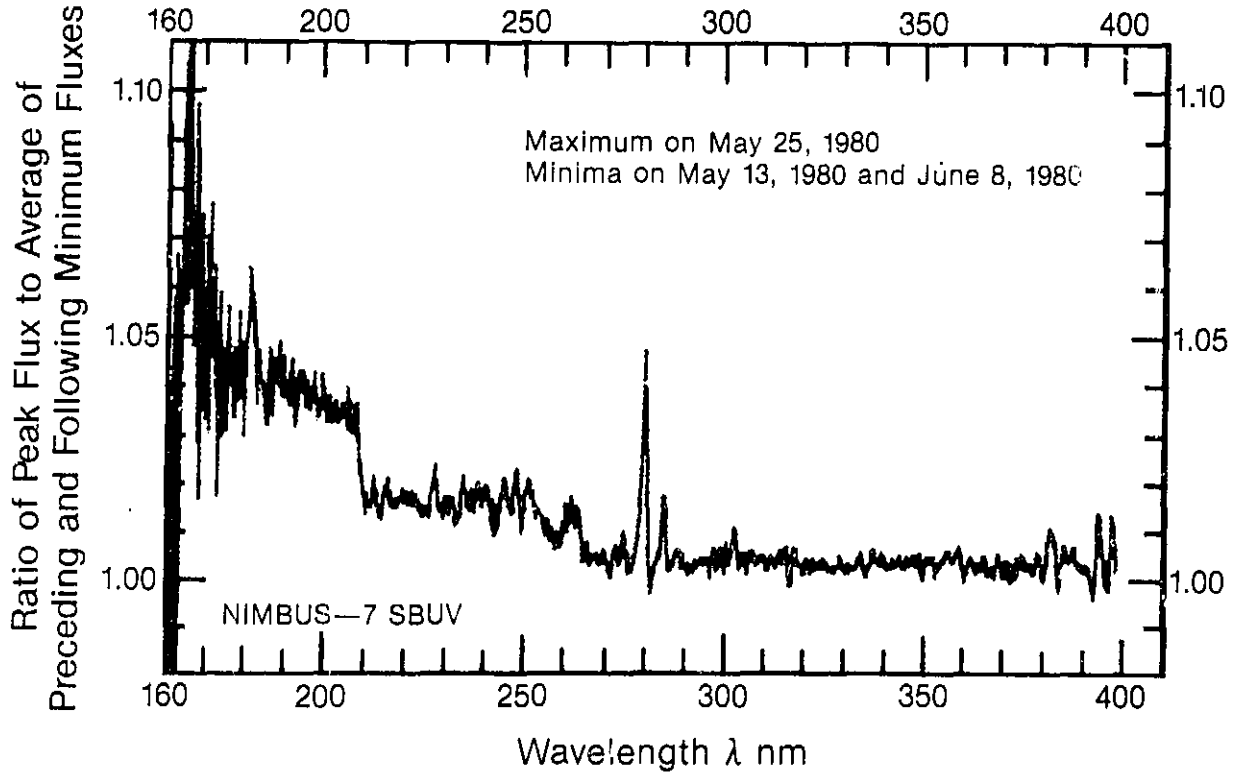

Figure 2.5 Spectrum of the Short-Term Variation that Peaked on May 25, 1980.

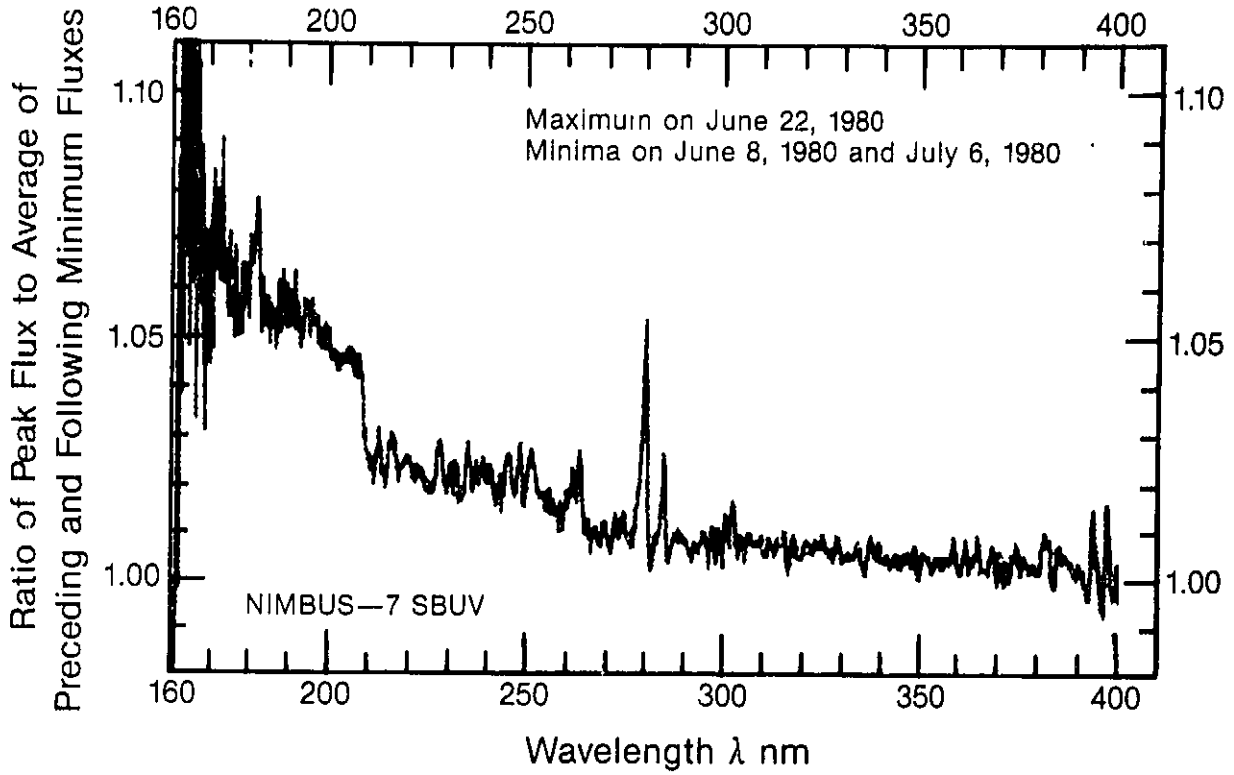

Figure 2.6 Spectrum of the Short-Term Variation that Peaked on June 22, 1980.

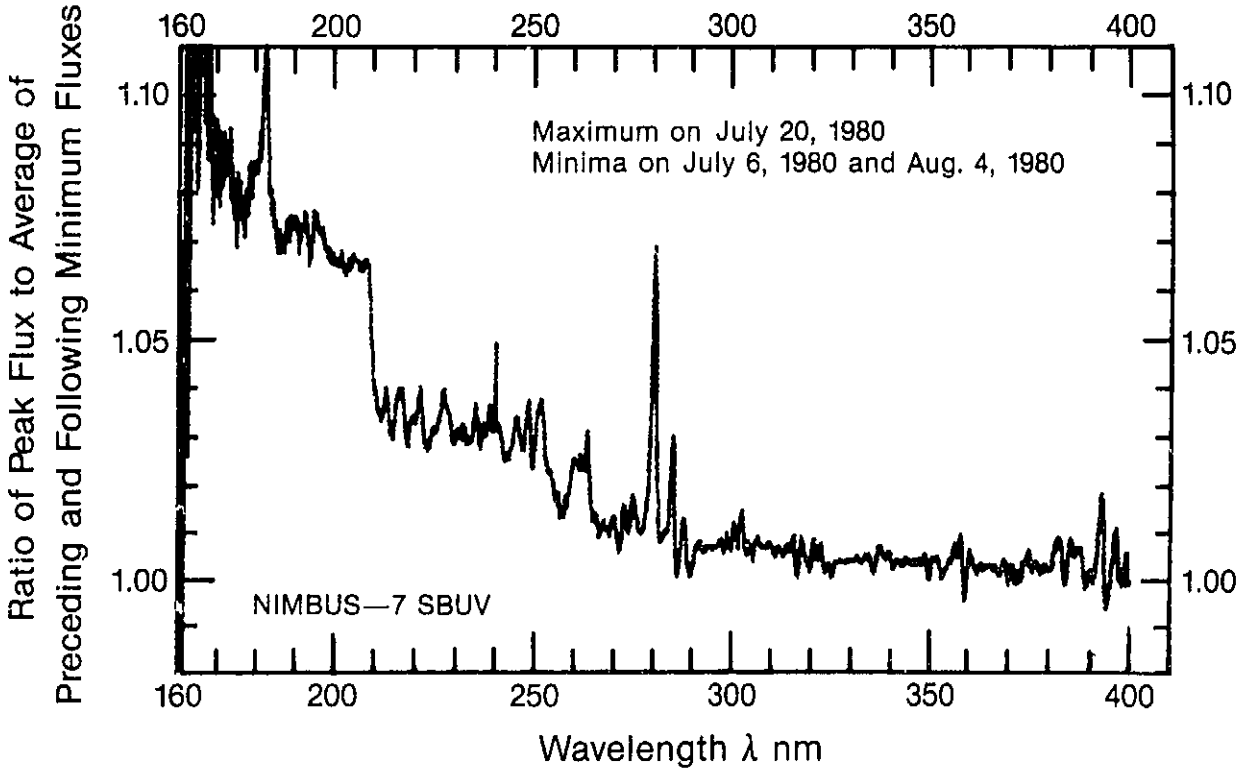

Figure 2.7 Spectrum of the Short-Term Variation that Peaked on July 20, 1980.

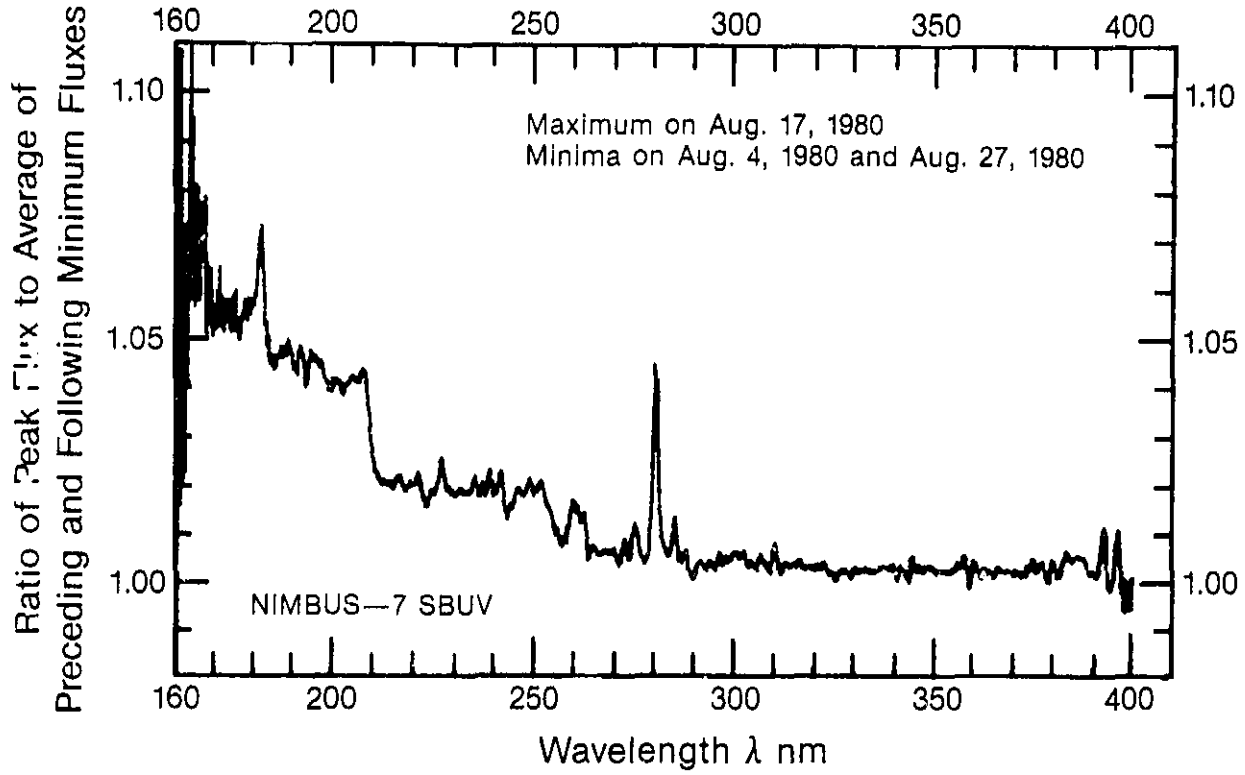

Figure 2.8 Spectrum of the Short-Term Variation that Peaked on Aug. 17, 1980.

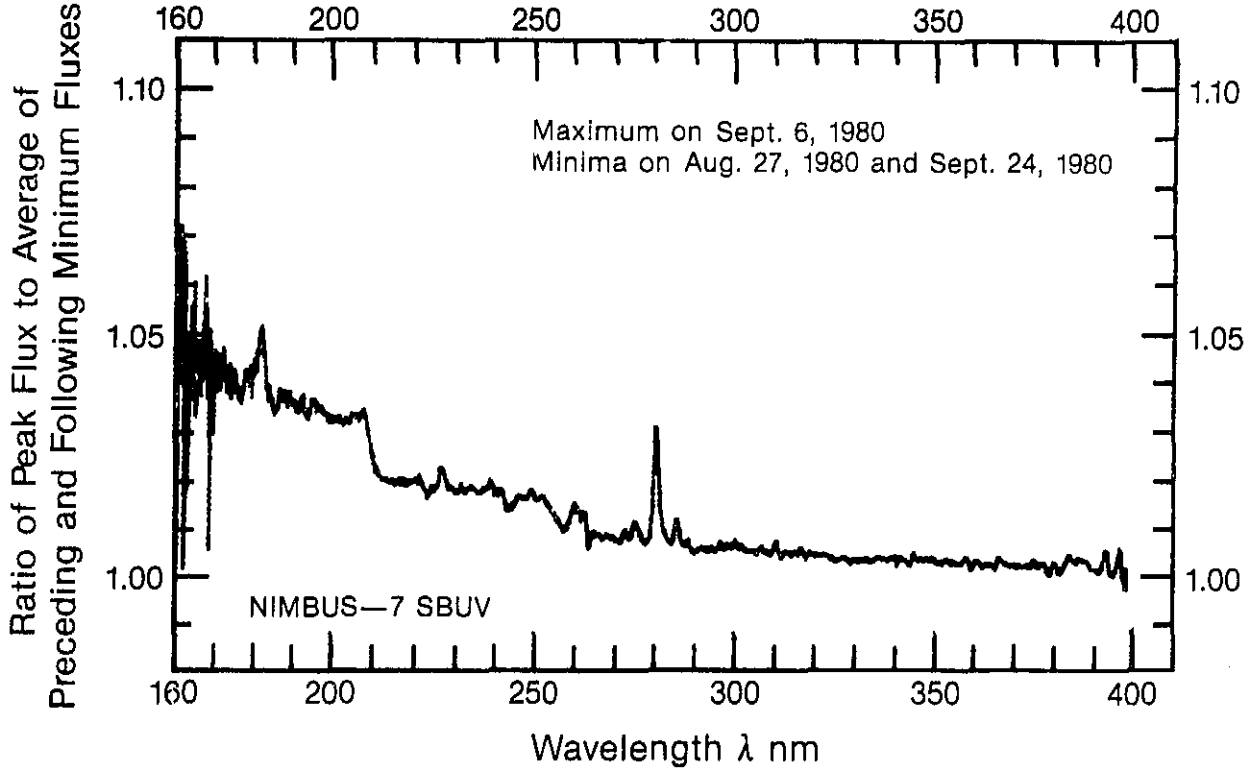

Figure 2.9 Spectrum of the Short-Term Variation that Peaked on Sept. 6, 1980.

Besides these common features, there are some differences among the eight cases shown in Figures 2.2 - 2.9. The simplest difference is that there is a range in intensity from the small variation in Figure 2.9 to the large variations in Figures 2.3 and 2.7. The smallest case in Figure 2.9 is as large as the average of 15 variations observed during the first year of NIMBUS-7 observations and studied by Heath et al. (1983). A second difference is that the ratio of the percent enhancement of the combined Mg II H and K lines at 280 nm above the adjacent wavelength background to the percent enhancement of the Al I continuum head near 205 nm above the variation at wavelengths just longer than the continuum edge (210 nm) varies from one case to another. The Mg II lines to Al I continuum ratio is low in Figure 2.2 and high in Figure 2.5. Similarly, the ratio of the enhancement of the Si II group of lines near 182 nm above the variation at adjacent wavelengths to the Al I continuum enhancement varies among the eight cases, also being lowest in Figure 2.2 and highest in Figure 2.5. We interpret such secondary effects to mean that the plages that contribute to these short-term variations have differences in their distributions of temperature differential emission measure (electron density squared integrated over all volumes with temperature in the range T to T + dT) as a function of temperature. For example, some of the dominant plages that produce the short-term maximum involved in Figure 2.5 have stronger enhancements in the temperature range important to the plage emission in the Si II and Mg II lines relative to the lower temperature region that dominates the plage emission in the Al I continuum.

Some differences among the eight cases are not real differences in the solar radiation but are artifacts of observational problems. Figures 2.3, 2.4, and 2.6 - 2.9 exhibit continuum-like ratios significantly greater than unity throughout the 265 - 390 nm wavelength range, which probably are not

real except for the clearly evident strong spectral lines. These ratios were computed using one daily average flux value for the preceding minimum and one for the following minimum in order to reduce the effect of the long-term instrumentation drifts. This technique for removing the long-term drift may be insufficient, particularly where the long-term drift is rapidly varying or nonlinear with time, especially if the maximum is not centered with respect to the preceding and following minima. The background curve in Figure 2.1 suggests that the cases in Figures 2.3, 2.4 and 2.6 - 2.9 involve such conditions. Continuum enhancements are discussed in detail in the next chapter.

Other differences possibly caused by observational problems are the differences in the Mg I line enhancement at 285 nm and the Ca II H and K lines among these eight cases. Note that when these line enhancements are particularly strong, there are some deep sharp valleys at adjacent wavelengths. Conversely, when these line enhancements are small, the background at adjacent wavelengths is smooth. Some of the apparent variation in these narrow absorption lines may be the result of a slight jitter in the wavelength drive.

An examination of the Ca-K plage observations published in Solar Geophysical Data shows that some of the plages that dominated the enhancement in Figure 2.2 also contributed strongly to the preceding maximum in October and to the following maxima in Figures 2.3 and 2.4. The October, November and January short-term peaks were dominated by plages in the northern solar hemisphere. The peak in December, 1979, involved a mixture of northern and southern hemisphere plages. The evolution of this sequence of peaks, and the others discussed below, involves plages lasting for a couple of solar rotations, but more importantly it involves the continued emergence of new activity in the same general vicinity as older regions but with enough difference in

plage shape or position that they are not labeled as being a simple continuation of a previous plage. Each short-term peak involves several plages in a fairly broad solar latitude range where the solar rotation rate varies with latitude. The actual temporal period of the UV flux caused by the group of plages appears to be linked to the rate of rotation of the solar longitudes of continued emergence of new activity rather than simply just to the differential rotation rate of the plages after they are once formed.

The maxima in Figures 2.5 - 2.7 involve mainly southern hemisphere plages. The maximum in Figure 2.8 again involved a mixture of northern and southern hemisphere plages while that in Figure 2.9 was dominated by northern hemisphere plages. The groups of plages that contribute to several quasi-periodic UV peaks with about a 28-day period tend to dominate the UV flux variations for episodes that last about 3 - 5 months.

The daily Ca-K plage index published in Solar Geophysical Data tends to vary in general like the short-term UV variations. The plage index data suffered from many days of missing data during January - May, 1980, and would not be very useful for estimating short-term UV variations for that period. A large discrepancy between the daily plage index and the short-term solar UV flux variations occurred when the index peaked on December 8, 1979, while the UV flux peaked on December 11. This difference may have been caused by Hale Region No. 16478, which had a very large area. The plage intensity factor applies only to the brigthtest part of the plage. If a plage is scaled with a very large area where most of it is not very bright and a small part of it contributes to a high intensity rating, then the influence of such a plage on the daily plage index (or the UV model of Lean et al., 1982) may be too strong because the area and intensity are multiplied as if the intensity applied to the whole area.

3. CONTINUUM VARIATIONS

In Figures 2.2 - 2.9, the aluminum absorption edge in the solar spectrum contributes the strong change with wavelength from about 207 to 212 nm. Much of the short-term variation at wavelengths shorter than 207 nm appears to be caused by changes in the Al I absorption. Numerous small lines also contribute in addition to the Al I continuum. We chose the 183 - 205 nm wavelength range to study the Al I continuum to avoid the strong Si lines at 182 nm and to avoid the continuum edge effects longward of 205 nm. It is not possible with the NIMBUS-7 observations with an effective bandwidth of about 1 nm to resolve all the minor lines and distinguish the contribution by minor lines from that due to the continuum. So we will analyze the combination of lines and continuum in the 183 - 205 nm range and refer to it as the effective Al I continuum.

In Figure 2.3, the rate of increase in the percent variation with decreasing wavelength below 207 nm is quite large while in Figure 2.9 it is much smaller. Part of this difference in the effective Al I continuum slope is simply caused by the variation in Figure 2.3 being larger at all wavelengths than that in Figure 2.9. One main question that we will pursue is whether there is more involved in the change in slope of the effective Al I continuum other than just that the change in the overall intensity.

A second continuum of interest is the Mg I continuum at wavelengths below about 251 nm. In this case, the presence of a real continuum separate from a combination of many absorption lines is not clear. Many lines of Al I, Fe I, Si I, and other constituents are present. We will refer to the 212 - 241 nm range as the effective Mg I continuum with the understanding that it is a combination of lines and continuum. Note that in Figures 2.2 - 2.9, the average over the 212 - 241 nm range is like a base level above which the Al I continuum rises. If much of the 212 - 241 nm enhancement is truly from a Mg I

continuum, then this Mg I continuum should extend to wavelengths shorter than the Al I edge near 210 nm; but this extension may not be a simple extrapolation of the level of the Mg I continuum at wavelengths longer than 210 nm. In that case, what we have called the effective aluminum continuum (183 - 212 nm) includes a Mg I continuum with an unknown amplitude that is probably comparable to or less than that near 212 nm.

If the relative shape of the fractional UV variation (the slope of the Al I continuum, the size of the rise at the Al I edge near 210 nm and the height of the effective Mg I continuum) remained the same in these figures but just varied by a multiplying factor "u" from case to case, then the ratio of the percent flux enhancement averaged over the 183 - 205 nm band to that in the 212 - 241 nm band should be a constant and the Al I continuum slope should be proportional to "u". Such a multiplying factor would result if the difference in magnitude from one rotational variation to another were simply caused by the addition of more plage area (without any change in the plage density as a function of solar altitude and temperature) at the longitudes that contribute to the rotational maximum peak or the reduction in plage area at the longitudes that contribute to the local minima. If the larger peaks involved changes in the plage density as a function of solar altitude and temperature rather than just variations in the net plage area, then the spectra shape involved in Figures 2.2 - 2.9 may change.

3.1 Continuum Slope Analysis

Figure 3.1 shows an example of the 183 - 205 nm band in detail for the solar-rotation variation shown in Figure 2.8. Linear regression analysis was used to fit the straight line shown to achieve the least sum of the errors squared. Table 3.1 lists the resultant slopes for the effective Al I continuum for seventeen cases of large UV variations. The first eight are cases

Table 3.1 Solar-Rotation Variations Analyzed

Date of Maximum	Aluminum I Continuum 183 - 205 nm Slope 10^{-2} % nm^{-1}	Aluminum I Continuum 183 - 205 nm Mean Percent Enhancement	Mg I Continuum 212 - 241 nm Mean Percent Enhancement
Jan. 3, 1979	-6.4	3.0	1.1
March 31, 1979	+3.0	3.1	1.8
April 16, 1979	-1.8	3.3	1.4
May 13, 1979	-2.3	3.0	1.3
June 7, 1979	-7.1	4.3	1.7
Aug. 25, 1979	-2.1	2.5	1.3
Sept. 23, 1979	-3.5	4.2	2.1
Oct. 18, 1979	-3.7	4.1	1.9
Nov. 13, 1979	-4.1	5.0	2.2
Dec. 11, 1979	-3.7	4.1	1.9
Jan. 6, 1980	-5.5	5.6	2.7
May 25, 1980	-3.4	3.8	1.6
June 22, 1980	-5.3	5.2	2.3
July 20, 1980	-4.5	7.0	3.3
Aug. 17, 1980	-3.8	4.4	2.0
Sept. 6, 1980	-2.4	3.5	1.9
Oct. 12, 1980	-2.6	2.6	1.0

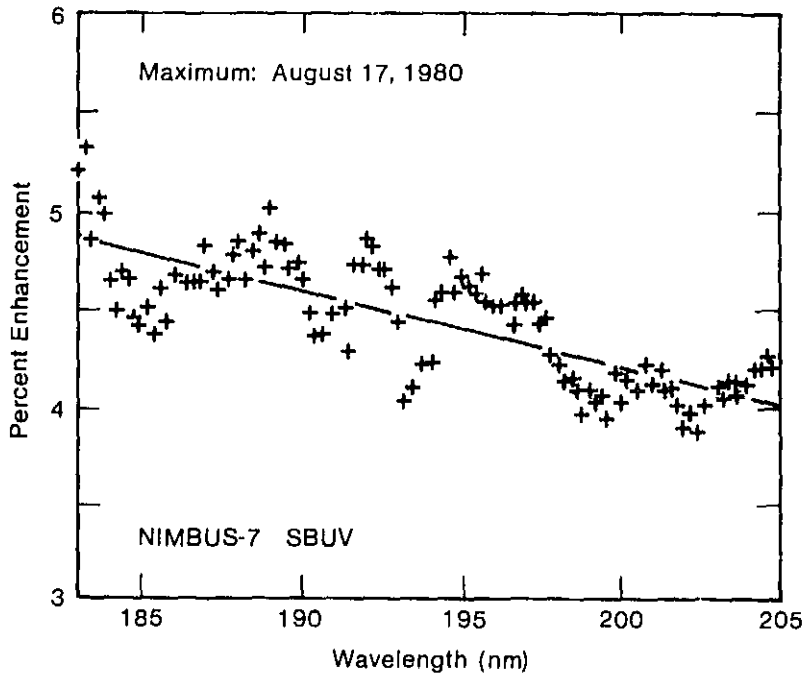

Figure 3.1 Spectrum of a short-term variation in the Al I continuum.

discussed by Heath et al. (1983). The second eight are the cases shown in Figures 2.2 - 2.9. The magnitude of the linear correlation coefficient for the flux ratio versus wavelength was in the range 0.34 to 0.81 (median = .68) and all seventeen cases were significantly correlated with respect to 95% confidence limits. Figure 3.2 shows that the slope of the effective Al I continuum is weakly correlated (r = 0.37) with the magnitude of the enhancement at those wavelengths. In order to examine the influence of the slope beyond that given by the linear relation, we will label those cases that are more than 10 % above the line to be large slopes for the net intensity involved, and those that are more than 10% below the line to be small slopes relative to the linear trend.

Figure 3.3 shows a similar analysis for the Mg I continuum range. Numerous lines are evident and it is not clear whether the valleys between them are still dominated by lines or by a real continuum. The continuum edge that should be near 251 nm is complicated by a group of lines of Fe and Si. Therefore, we do not have clear evidence in these observations of the presence of the Mg I continuum or the net strength of lines relative to the continuum. Linear regression analysis resulted in best-fit lines with nearly zero slopes. Furthermore, a linear fit to these data cannot be interpreted as being representative of a continuum slope. If just the valleys between the lines were used to estimate a line, poor line fits would result. Consequently, the mean flux ratio was used for the 212 - 241 nm band as a measure of its intensity and the slope was assumed to be essentially zero.

3.2 Comparison of the 183 - 205 nm and 212 - 241 nm Wavelength Bands

The percent enhancement averaged over the 183 - 205 nm wavelength band is shown as a function of the associated enhancement in the 212 - 241 nm band in Figure 3.4. Each point corresponds to one of the rotational variations listed

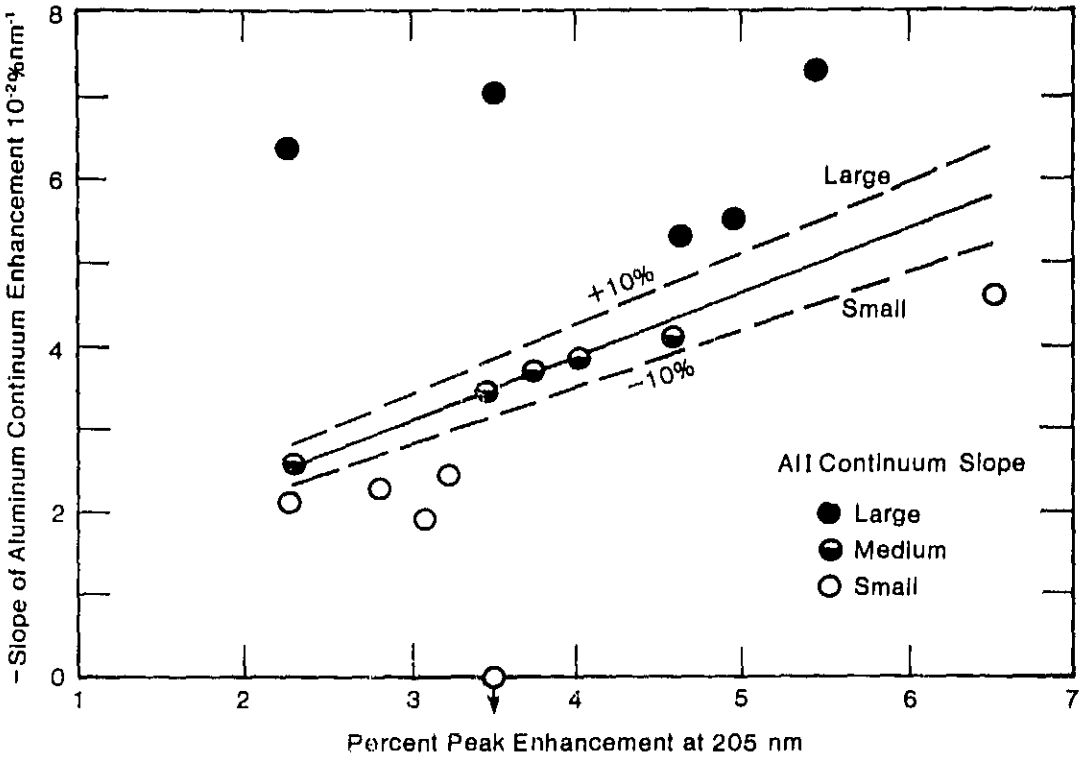

Figure 3.2 Definitions of large, medium and small slopes for the Al I continuum that take into account the relative magnitude of the short-term variations.

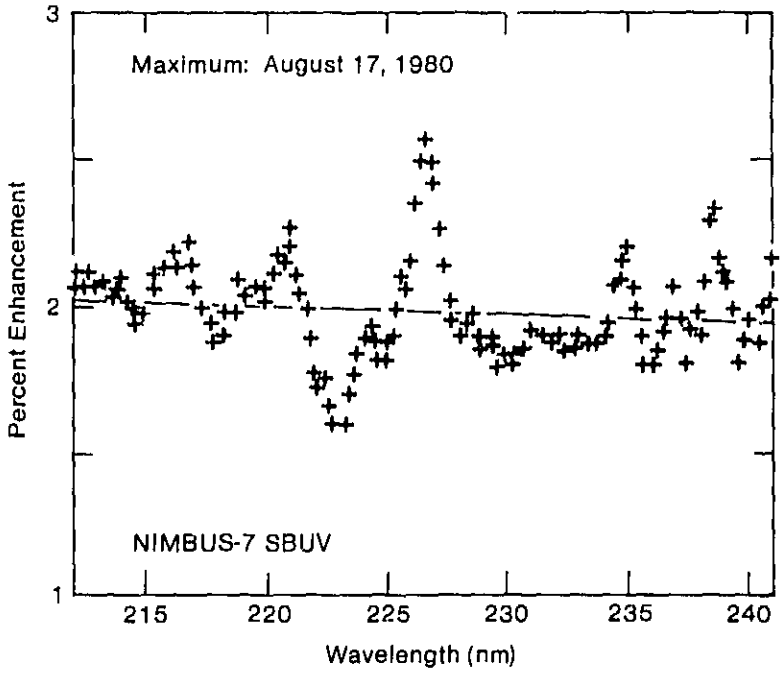

Figure 3.3 Spectrum of a short-term variation in the 212 - 241 nm range.

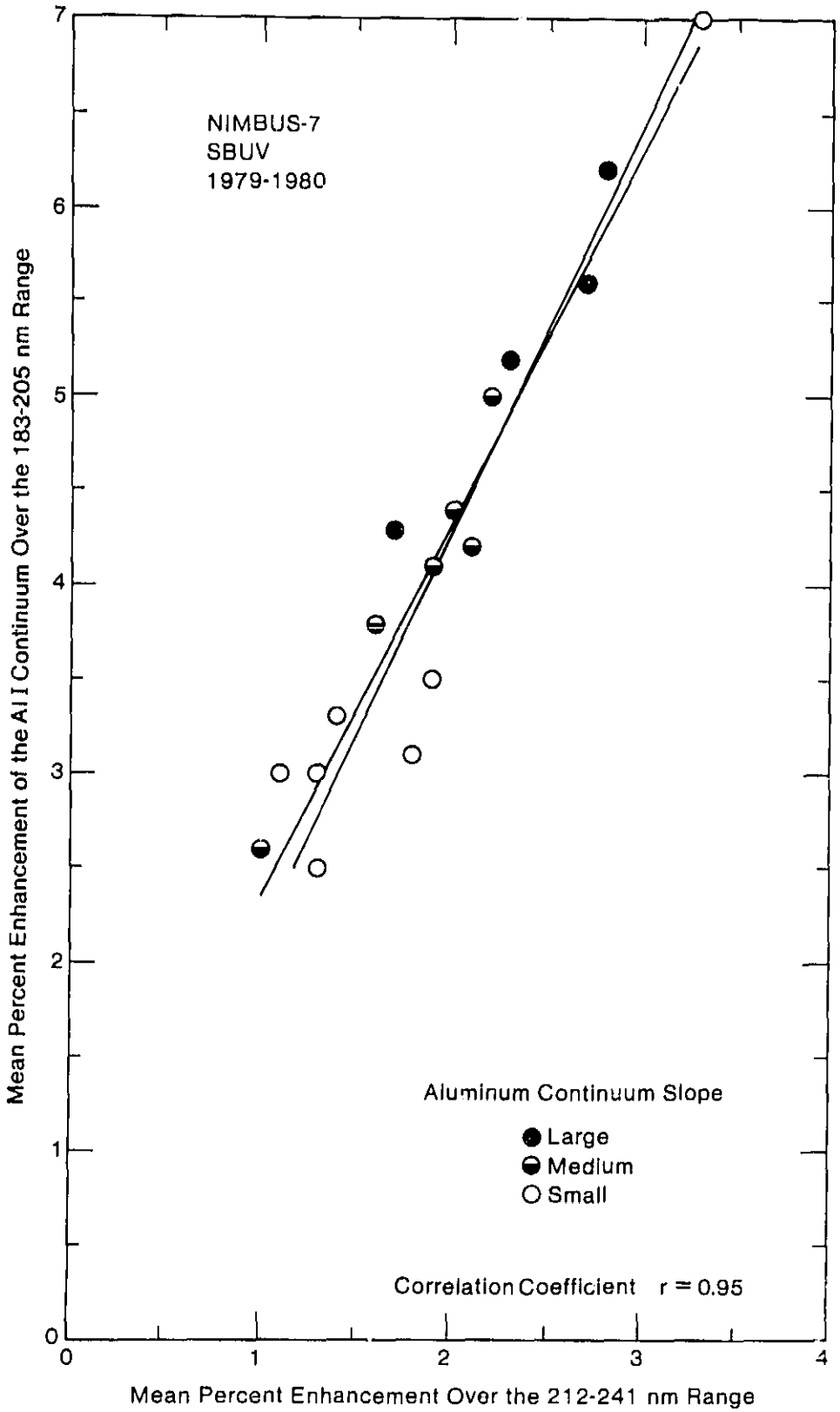

Figure 3.4 Enhancements in the Al I continuum compared to the 212 - 241 nm enhancement.

in Table 3.1. The two bands are highly correlated. The straight lines were fit to the data to achieve the least net squared error. The one line that happens to have a zero intercept indicates that the mean enhancement intensity in the 183 - 205 nm band is 2.15 times larger than that in the 212 - 241 nm band.

The linear trend is consistent with the short-term percentage enhancements being similar in spectral shape from one rotation to another but simply varying in amplitude, for example due to the net plage strength at the peak relative to that at the local minima. Any effects due to changes in the shape of the wavelength spectrum are second order relative to the linear trend. The wider scatter of points at the lower intensities may result from unknown observational errors that have a larger relative effect at small amplitudes.

The scatter with respect to the linear relation appears to have a dependence on the slope of the Al I continuum since the points for rotational variations with strong negative slopes with respect to wavelength tend to lie along the left side of the group of points while the points furthest to the right of the linear trend are cases with small slopes in the Al I continuum. It is reasonable to expect that such cases with small slopes in the Al I continuum would have a smaller rather than larger than average mean intensity enhancement averaged over the 183 - 205 nm band, and vice versa. This could result from variations in the distribution of plage density as a function of temperature and altitude in the solar atmosphere, the larger slopes corresponding to greater increases at the higher altitudes in the upper photosphere and chromosphere.

Figure 3.5 shows the ratio of the percent enhancement averaged over the Al I continuum to that averaged over the "Mg I continuum." Again, for small enhancements, the cases with large slopes tend to be at the top of the diagram

and those at the bottom have small slopes. The mean ratio in Figure 3.5 is 2.22 for all the cases, 2.36 for the large slope cases, 2.27 for the medium slope cases, and 2.05 for the small slope cases. These results suggest that a second order effect exists in the relation between the Al I continuum and the "Mg I continuum" band where their ratio is larger for cases with large negative slopes in the Al I continuum.

In Chapter 2, we pointed out, for example, that the high background level in the 267 - 325 nm range in Figure 2.3 is suspected of not being real but being caused by instrument drift and data analysis problems. That problem appears to be a larger source of relative error in the effective Mg I continuum enhancement than in the effective Al I continuum. Such errors would shift the position of a couple of the data points in Figures 3.4 and 3.5, but do not appear to affect the main trends discussed above. However, the percent UV enhancement involves a small difference calculation with the NIMBUS-7 data. The ratio of two bands like that in Figure 3.5 involves two small difference calculations and the comparison of individual ratios with the mean is in effect another small difference calculation. Small difference calculations can greatly increase the relative influence of observational errors. Therefore, we suggest that the above discussion of a second-order dependence on the Al I slope is evidence for such a dependence but does not prove it. Independent corroborating measurements are needed.

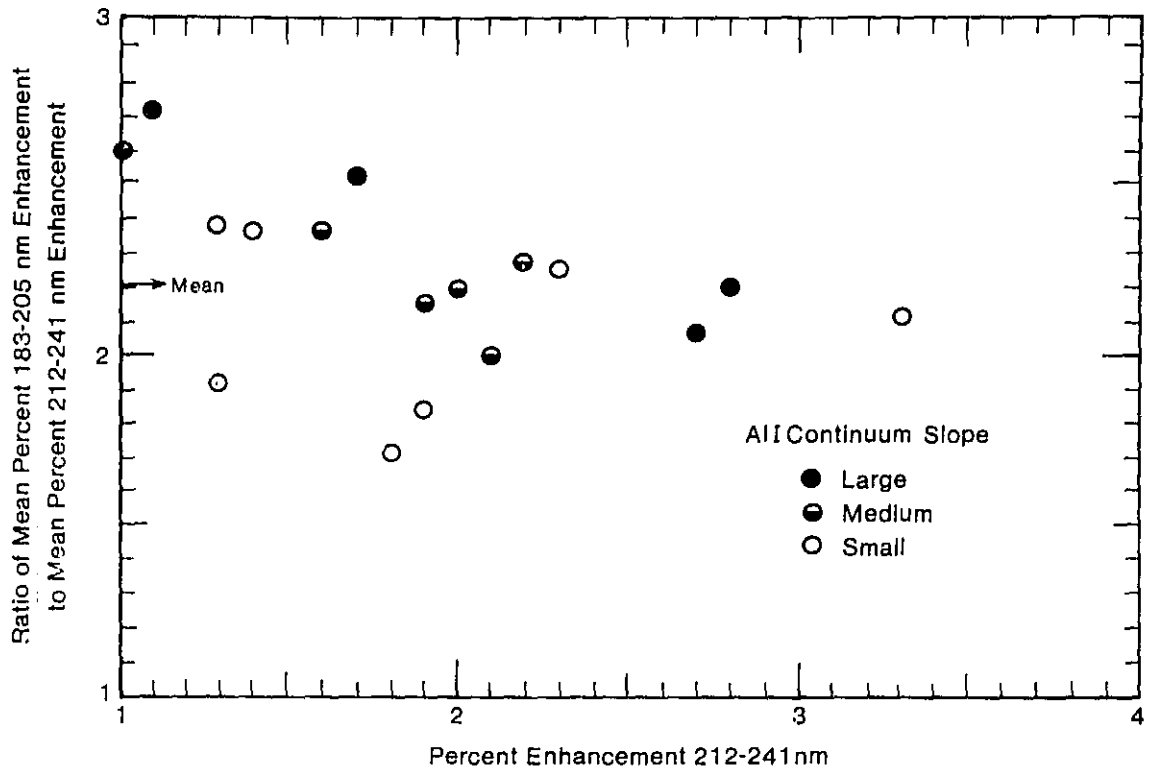

Figure 3.5 Second order effects as a function of the Al I continuum slope in the relation of the Al I continuum enhancement to the enhancement in the 212 - 241 nm band.

4. LONG-TERM TREND AND NOISE REMOVAL

This chapter examines important features such as trends, discontinuities, noise, and outliers. The classic analysis of time series aims at separating an observed series into four sources of variation (Hald; 1956):

(1) A trend component: any systematic or long term change in the level of a time series.

(2) A cyclical component: any variation defined by a systematically recurring, not necessarily periodic, series of events.

(3) A periodic (sometimes called seasonal) component of known, deterministic period.

(4) A stochastic (random) component.

The first step in analysis is inspection of the available time series data. Figure (2.1) shows six time series from the NIMBUS-7 data. Units are in 10^{-3} Watts m^{-2} nm^{-1}. Each series in this figure consist of the daily averages of a particular spectral line or continuum in solar (UV) irradiance. The sampling period covers November 7, 1978 to November 1, 1980. The unit of time used is one day but the interval between successive observations is not constant.

Both the Si-II line and Al-I continuum display strong and almost linear fall off with time. Superimposed on this trend is a weak biannual oscillation combined with episodes of twenty-eight day and thirteen-day variations. A weak four-day variation is seen beginning on January 23, 1980.

The Mg-I and Mg-II lines also display linear fall off with time. The biannual oscillation is stronger and combines with a weak annual oscillation. Episodes of twenty-eight and thirteen-day events are strong in the Mg-II H&K line but have small amplitudes in the Mg-I line. The four-day component beginning on January 23, 1980 appears very strong in the Mg-I data.

The Ca-II H and Ca-II K lines show no linear trend. Most of the variance

is contained in an annual oscillation combined with a weak biannual oscillation. The series are noisy and contain many spikes. Episodes of twenty-eight day events are very weak and the thirteen-day episodes are either obscured in the noise or gone. The four-day component is still visible. Prior to any further analysis, including spectral analysis, these problems must be corrected or removed.

4.1 Identification and Removal of Fourth Day Variation

The four-day component has been identified as an instrumental phenomena not of solar origin. In the first year, all on-board experiments were usually turned off every fourth day. In the second year, the UV measurements were continually taken while other experiments were turned off on the fourth days. This introduced an anomalous operating temperature into the system which offsets the measurements on every fourth day from the surrounding three days.

The fourth day component appears in all six time series, but is strongest in the Mg-I line. Measurements taken on these days are, at this time, unreliable data points. To determine their pattern of recurrence, time plots of all six series were blown up. Starting on January 23, 1980, every fourth day in each series is repeatedly low. These data points were removed.

After removal of these points, time plots were again generated. The Si-II line, Al-I continuum, and Mg-II H&K lines showed the problem had been removed. However, the Mg-I, Ca-II H, and Ca-II K lines all show the day following the main fourth day low also tends to be slightly low. This is most evident in the Mg-I line. At present there are no explanations for this minor second fourth-day problem. These data points were not excluded from analysis.

4.2 Identification and Removal of Spikes

Also present in the data are spikes. A spike is defined to be a single

point that is far greater than the rest in absolute value. That is, it lies three or four standard deviations or further from the mean of a stationary series.

Spikes cause numerous problems in analysis and modeling. Two such points close to each other introduce spurious frequencies into the power spectrum and cross spectrum. It is necessary to remove these points before proceeding. Unfortunately, there are no general procedures for automatic elimination of outliers.

It is important to note that positive spikes may be perfectly valid observations. Solar flares, which are brief high-energy outbursts, may cause these events. Alternatively, positive spikes may be spurious observations arising, for example, from shot noise in a photomultiplier tube. But no known solar process will cause negative spikes. In cases where a spike is determined to be anomalous, the spike must either be adjusted to its expected value or simply removed.

There are a number of schemes for removing spikes. One method is to use digital filters which produce smoothed (lowpass filtered) estimates of the original data point. There are complications with this procedure. One complication is that after several spike detections in a row, the smoothing can wander far enough away from the real data so as to reject good data. In this analysis, spikes are removed.

The first objective in spike identification is to stabilize the mean. This is most easily achieved by sufficient differencing. Differencing a time series amounts to subtracting a given observation from its nearest neighbor. The procedure is then repeated until the time series displays a constant mean (called stationarity in the mean). Box and Jenkins (1970) point out that first differencing will remove all linear trends and long term oscillations.

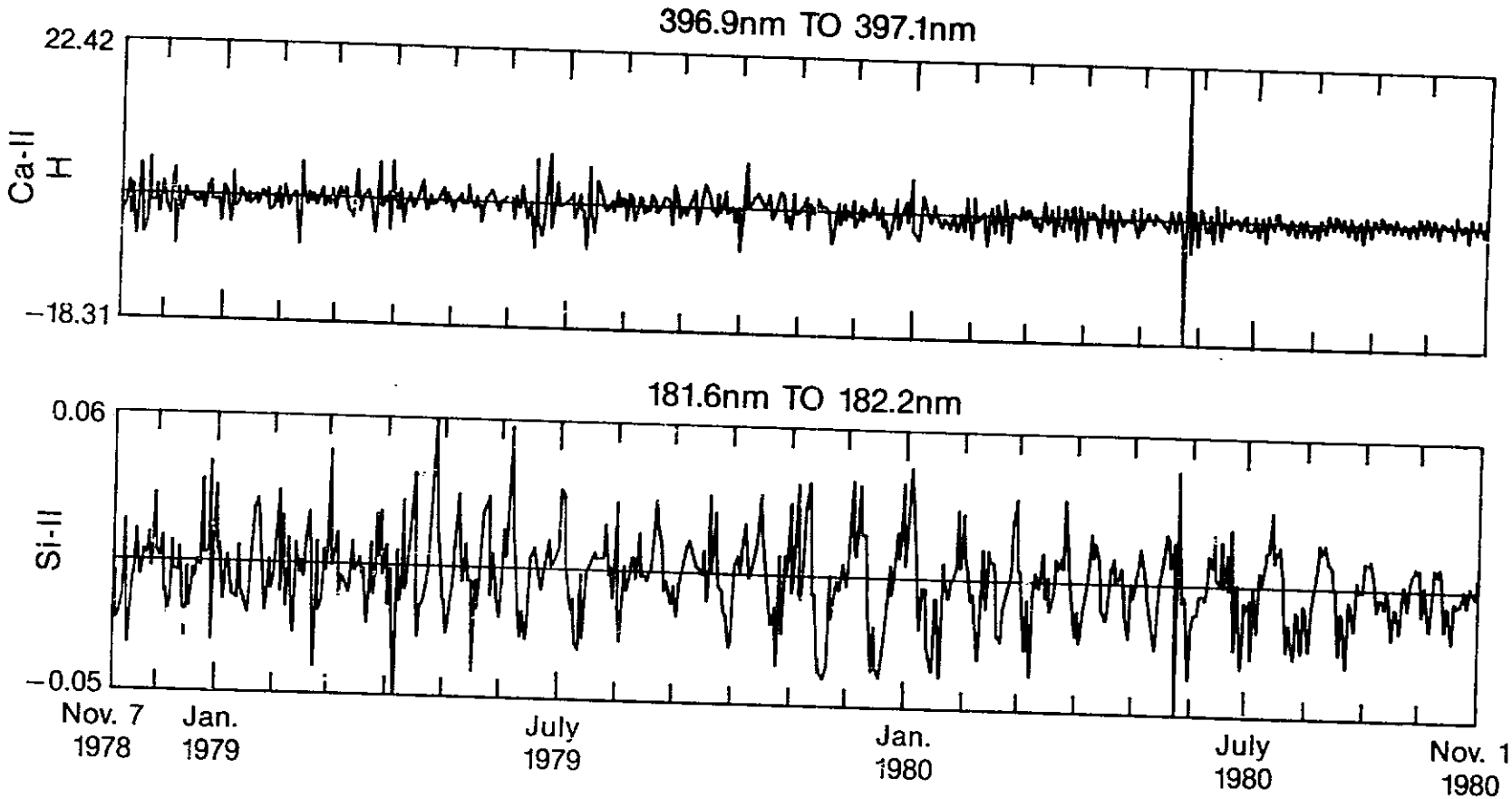

Figure 4.1 First difference of Si-II line (top) and Ca-II H line (bottom).

Second differencing will remove all short term non-periodic components. It is usually sufficient to difference a series twice.

Figure 4.1 shows the first difference of the Si-II and Ca-II H time series. The fourth day noise has been removed from the original time series. Note that all long term trends are now gone. However, short term variations remain and now contribute strongly to the variance. A second difference is called for.

Figure 4.2 shows the second difference of Si-II and Ca-II H. The minus three standard deviation line and plus four standard deviation line are shown. Note the series are now stationary in the mean. A very large spike appears in both series toward the end of May 1980. In addition there are several smaller spikes distributed over both series.

When a series containing a spike is differenced once, the spike becomes a neighboring pair of spikes with opposite signs. If the spike were positive in the original series, it becomes a positive spike followed by a negative spike. Negative spikes have just the opposite pattern. The spike in May 1980 is a negative spike and its first difference shows this structure in figure 4.1.

If the first difference does not produce a series constant in mean, difference it again. In the second difference, a spike that is positive in the original series now has the signature of a positive event followed by a large negative event followed by a positive event. Again, a negative spike has just the opposite structure. Figure 4.2 shows this structure for the second difference of the spike of May, 1980.

The procedure that was applied to all series in the NIMBUS-7 data set is to:

(1) Compute a second difference.

(2) Compute the standard deviation for the second difference series.

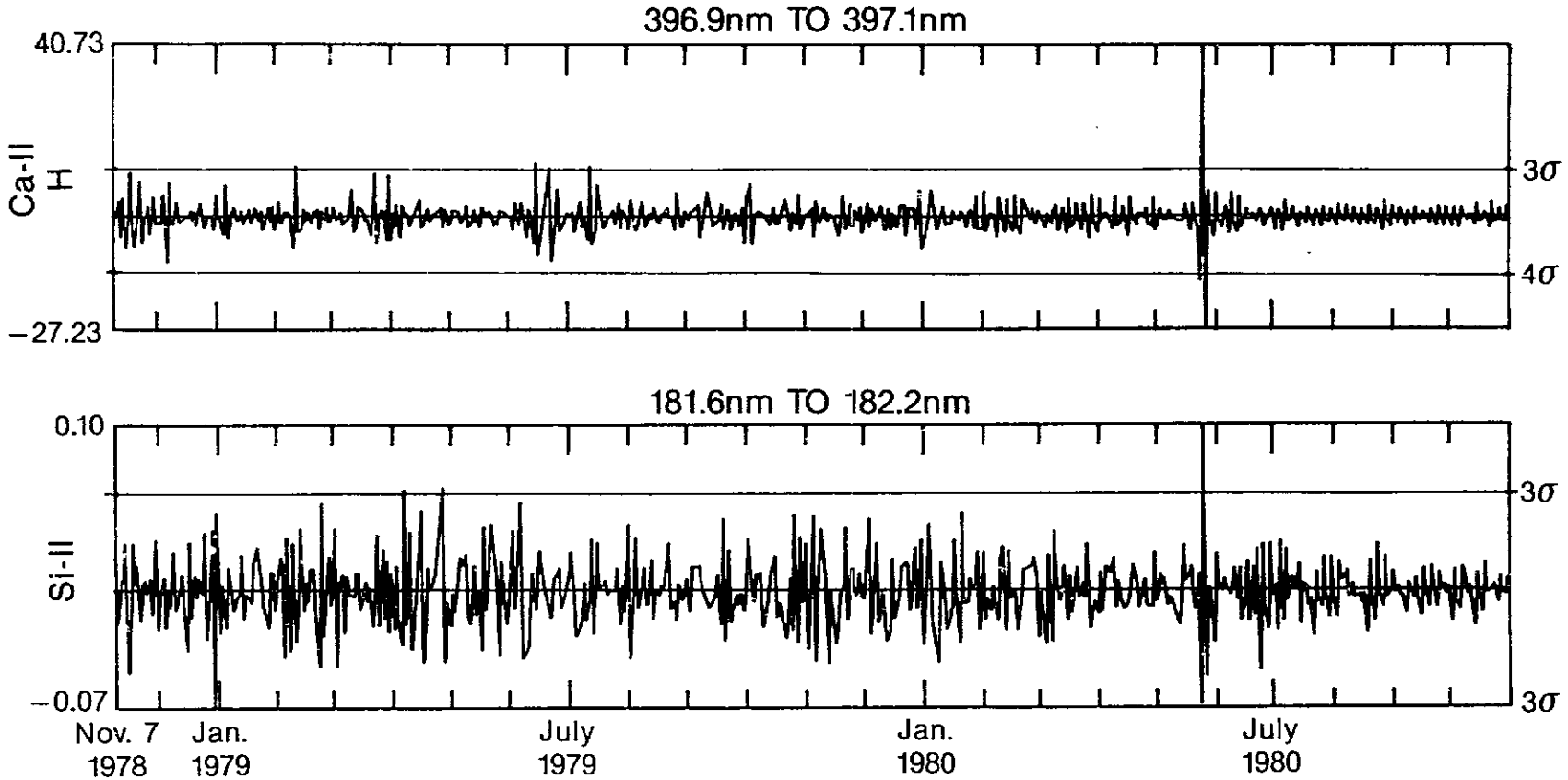

Figure 4.2 Second difference of Si-II line (top) and Ca-II H line (bottom).

(3) Search for a spike by comparing the sign on three neighboring observations. If a plus-minus-plus pattern occurs there is a positive spike in the original time series (just the opposite pattern for a negative spike).

(4) Compare the absolute magnitude of the spike to a pair of preset thresholds. Note that because we can discriminate between positive and negative spikes we can set two different thresholds.

(5) If the magnitude exceeds the threshold, go to the original time series and remove that point.

(6) If a data point was removed, repeat the procedure starting at step 1. If no spikes exceed the thresholds, you are finished.

The method has several advantages. It is a simple and fast procedure that is very sensitive to spikes. Because positive spikes may be of solar origin we can desensitize the procedure by setting a high positive threshold. Four standard deviations was used and we note that no positive spikes were removed from any of the series at this threshold. But negative spikes are likely to be spurious observations. A negative threshold of three standard deviations was set. Several points, including the event in May 1980, were eliminated.

The procedure will only remove spikes as defined above. If two or more points together are outliers, the procedure will not eliminate them. These define level changes and are left in the data for further investigation. Such an event occurs over the first few days in October 1979. With the four day component and major spikes removed, we next turn to analysis and removal of long-term variations.

4.3 Removal of Long-Term Variation

Variation in the NIMBUS-7 data is dominated by long term change in the mean. The behavior of this variation changes with wavelength becoming less

linear as wavelength increases. We know that part of this variation is due to diffuser degradation. Other aspects of the undulations may be due to long-term solar variability. At this time, the information needed to separate the instrumental drift from long-term solar variability is not available.

This analysis has as its objective the modeling of local variations due to solar rotation. The structure of these local variations can be examined by removing the long-term trend component. There are a number of techniques for removing long-term undulations in the data. Common procedures include filtering, moving averages, differencing, and orthogonal polynomials.

If there is no interest in the functional form of the long-term variation, high-pass filtering may be applied. High-pass filtering converts the original time series into a new series consisting of all information on a specified frequency range (B = pass frequency to F = folding frequency) while rejecting all information in the range (0 to B).

Filters, however, do not behave well. They tend to fold information from the band-reject region into the band-accept region, and phase shift the data. Also, filters cut [1/(2B)] data points from each end of the time series thus reducing the number of observations. To get an efficient filter requires not only this cost be paid but also long computation times.

Moving average methods are examples of high-pass filtering. Kendall (1976) describes the method. The method has the advantage over other filters in that it does not phase shift the data. But it has major problems in that a large amount of variation from the band-reject region is passed into the band-accept region. In addition, data is cut from each end of the time series. For these reasons we have decided not to filter the data.

The technique of differencing has already been discussed. We have seen

that it provides a method for removing the long term trends. But often it is very difficult to physically interpret a differenced time series. Differencing is most useful in prediction. Its chief advantage over all other methods is that it allows the building of a dynamic model which accounts for what appears to be (and may actually be) a trend. As there is some interest in forecasting, the differencing approach will be applied.

Figure 4.3 shows the result of first differencing the data after spikes and fourth day events are removed (units are Watts per cubic cm). All long-term variation has been removed. The data appear very noisy. Episodes of twenty-eight and thirteen-day variations are still visible in the Si-II, Al-I continuum, Mg-II H&K, and weakly in the Mg-I line. We can see no episodes in the Ca-II K or the Ca-II H lines.

To aid in the physical interpretation, the method of orthogonal polynomials will also be applied. It is a regression technique that models long-term movement in a time series. The number of terms in the polynomial can either be specified prior to fitting, or an iterative stepwise procedure can be applied. This stepwise procedure begins with a zero order polynomial, that is, the mean. A variance is computed. Then a first-order model (i.e. linear regression) is applied and a residual variance computed. The steping continues to higher order polynomials until either no change occurs in the residual variance, or until all the long term variation that the analyst wants removed has been removed.

As with all regression techniques, the estimated polynomial can not be used for prediction outside the range of the data. It is a tool used simply to gain control on long-term variations. It has the advantage that each component in the polynomial can be examined to see how it contributes to total variation. This may have its use in gaining control over instrumental

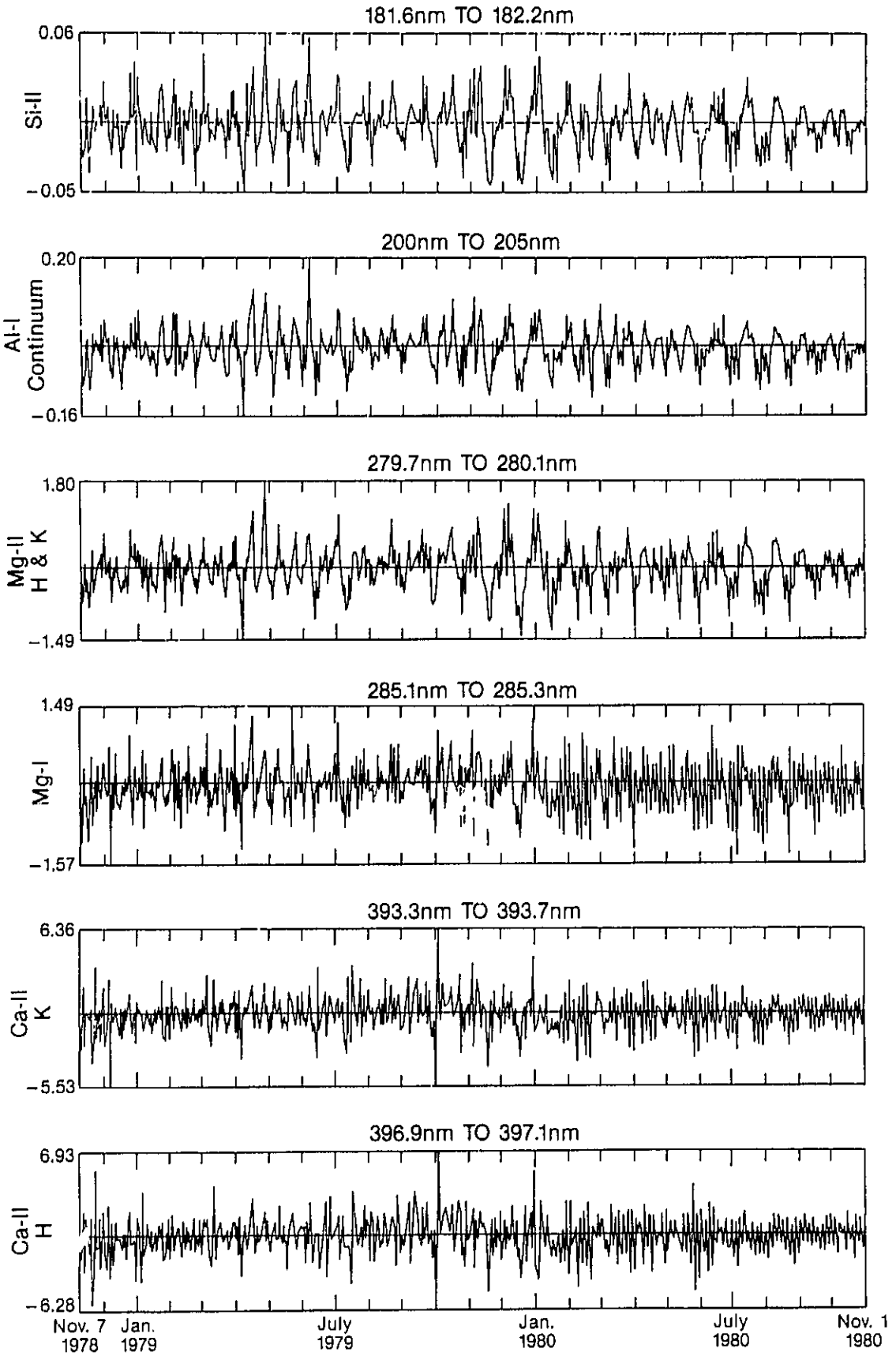

Figure 4.3 First differenced NIMBUS-7 data (spikes and noise removed).

drift. The method also does not phase shift the data nor are any data lost.

Analysis began by applying a simple linear detrend to the data. We found that there still remained substantial variation from a roughly annual and biannual variation. The variance decreases markedly up to a third-order polynomial, and slowly thereafter. However the third-order polynomial still missed the annual and biannual oscillation. The order of the polynomial was increased until the only variation that remained was smaller than 120 days. The degree found that produced the best result was a twelve-degree polynomial. Figure 2.1 show the fitted polynomials. Figure 4.4 shows the data after the respective trends devided out, thus removing the physical dimension.

These data are less noisy than the differenced data. Twenty-eight and thirteen-day variations are seen in the Si-II line, Al-I continuum, and Mg II H&K lines. These variations are also seen in the three other lines, but are weak. Noise remains in these other three lines. There also appears a ninety-day variation that appears during the episodes of thirteen-day events.

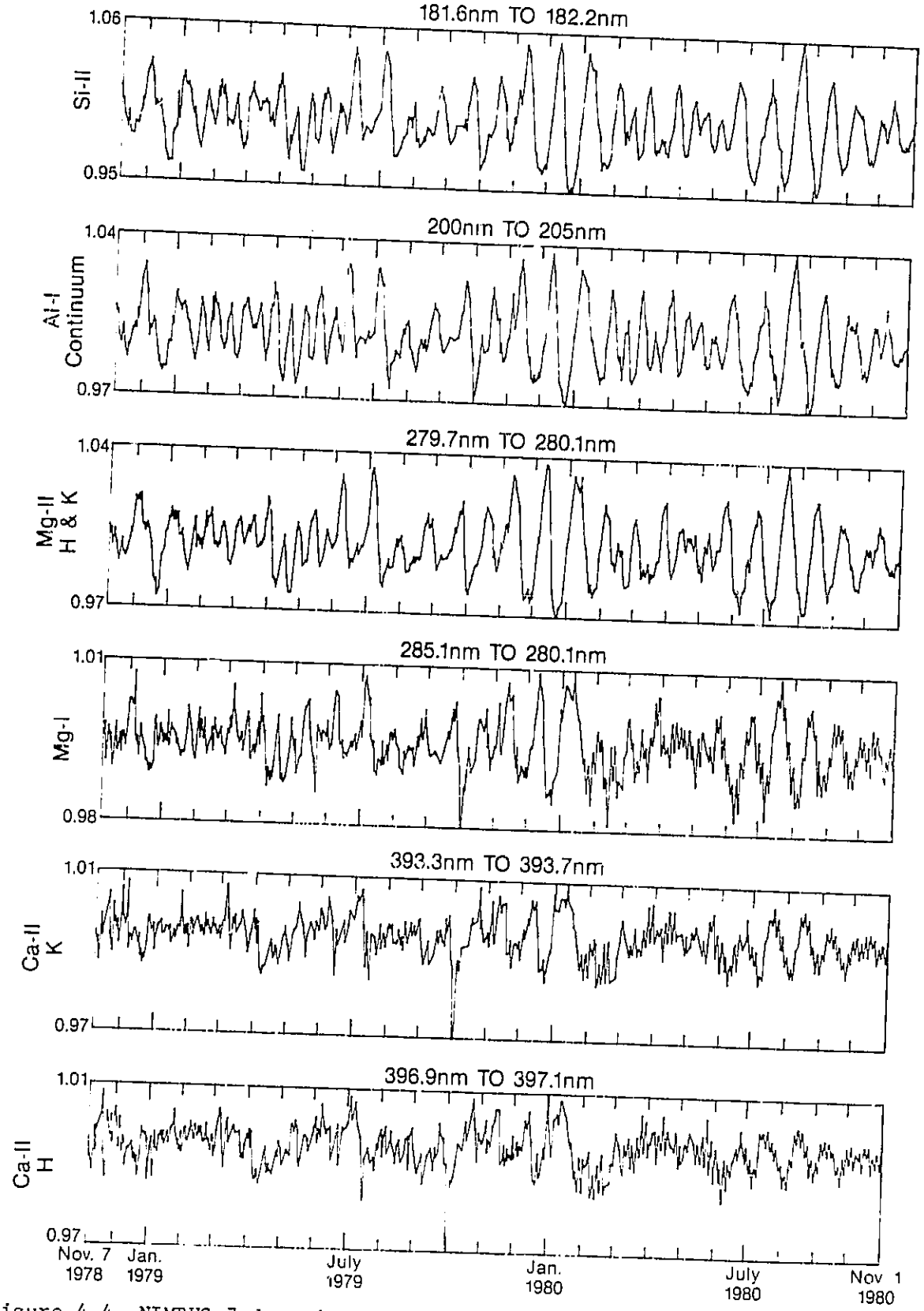

Figure 4.4 NIMBUS-7 data detrended by twelve-degree orthogonal polynomials.

5. AUTOCORRELATION AND SPECTRAL ANALYSIS

Variability in solar ultraviolet (UV) spectral irradiance will be examined using basic concepts and tools of univariate (single variable) time-series analysis. Analysis will be applied to both the polynomial detrended data set and the first differenced data set. Techniques from both time domain, following Box and Jenkins (1976), and frequency domain, following Bloomfield (1976), will be applied to each data set. This dual approach is utilized because complex processes often display confused, hidden, or distorted behavior patterns. Representation of a process from two different perspectives often reveal detailed structures that might otherwise be overlooked.

Time-series analysis provides a methodology to evaluate complex linkage patterns within phenomenon that extend across space or time. Chiefly, the technique models change in phenomena. It is an iterative procedure which begins in a preliminary stage that examines time plots of variables used to characterize the phenomenon under study. This stage was completed in the last chapter. Then, using tools developed in this chapter, the time and frequency structure of these variables are evaluated. From these results an initial approximation to the process can be made.

5.1 Method

The principle underlying time-series modeling asserts that influence of a past event on the present diminishes with time. In time-domain analysis, the methodology consists in constructing a model which characterizes the correlation of a process with itself at different times, past or future. In the frequency domain, the methodology consists in constructing a Fourier model which characterizes the energy content (or variance) of the processes in terms of sinusoidal components.

These two methods are mathematically equivalent (Chatfield; 1982). The standard tools for this preliminary analysis are the estimated autocorrelation function, partial autocorrelation function, and power spectrum.

For our purposes, a univariate time series is a sequence of observations ordered in time. That is:

$$X(t) = \{x(1), x(2), \ldots, x(N)\}$$

where (N) is the total number of observations, (t) is an integer index ($1 \leq t \leq N$) that represents the time at each observation, and x(t) is an observed value from a random process with a range of possible values. Accordingly, for each value of (t), x(t) has some probability distribution.

Standard time-series analysis assumes the distance $(t_i - t_{i-1})$ is constant. But, as noted in the last chapter, some real life situations do not permit data to be sampled at a constant rate. The following development and analysis assumes that missing observations occur. The approach utilized follows a method developed by Jones (1971). It is irrelevant to this method whether the missed data are caused by some known deterministic procedure or by some random mechanism.

5.2 Time Domain Analysis

The autocorrelation (or autocovariance) function provides information about how a process correlates (or covaries) with itself through time. It describes the dependence pattern among the observations of a time series. The method computes the correlation (or covariance) among observations separated by time (k). This separation time is called the "lag" and takes values $\{k = 0, 1, 2, \ldots, N - 1\}$. When the correlation (or covariance) between observation x(t) and observation x(t + k) are plotted against (k), we

obtain a graphical representation of how future and past observations depend on one another. Remember, standard statistical techniques require independent observations. Autocorrelation analysis allows us to get a handle on the dependencies among the observations. Knowledge of this structure can then be used in further modeling or analysis.

To compute the autocorrelation function, we assume X(t) to be weakly stationary. A process is stationary if its statistical properties do not change over time. That is, the probability of observing a specific value is independent of time, or, the random variables x(t) must have the same probability density function for all values of (t). Weak stationarity does not require the probability distribution for x(t) be identical to the probability distribution for x(t + k). All that is required is that their mean and variance be the same. Stabilization of the mean was the purpose behind detrending and differencing. Nonstationarity in the variance will be discussed later.

To estimate the autocorrelation function of a series that has no missing observations, we pair together observations separated by k days. There will be (N - k) different pairs. An asymptotically unbiased, consistent estimator for the autocovariance function is given by Priestley (1981):

$$C(k) = [1/(N - k)] \sum_{t = 1}^{N - k} [X(t) - \bar{X}][X(t + k) - \bar{X}] \qquad k = 0, 1, 2, \ldots, (N - 1)$$

But detrending the series produces a zero mean process. So the covariance reduces to:

$$C(k) = [1/(N - k)] \sum_{t = 1}^{N - k} X(t)X(t + k) \qquad k = 0, 1, 2, \ldots, (N - 1)$$

And the autocorrelation may then be estimated from this last equation by:

$$R(k) = C(k)/C(0) \qquad k = 0, 1, 2, \ldots, (N - 1)$$

NIMBUS-7 data were collected over a time span of N=721 days, except that some of the observations are missing. When observations are paired together, some pairs will contain missing observations. Thus there will not necessarily be (N - k) pairs at lag (k). The estimator of the autocovariance and autocorrelation functions given above will not work. To adjust the estimator for missing observations an indicator series is defined as follows:

$$I(t) = \begin{cases} 1 \text{ if } x(t) \text{ is observed.} \\ 0 \text{ if } x(t) \text{ is not observed.} \end{cases}$$

The observation times are known so that I(t) can easily be determined in post processing. Next the mean is removed from the time series and zeros are inserted into the series whenever a value is missing. An asymptotically unbiased estimator of the autocovariance function is then obtained (Jones 1971, Parzen 1963):

$$C(k) = [1/Q(k)] \sum_{t=0}^{N-k} X(t)I(t)X(t + k)I(t + k) \qquad k = 0, 1, 2, \ldots, (N - 1)$$

where:

$$Q(k) = \sum_{t=0}^{N-k} I(t + k)I(t)$$

Note that Q(k) must be greater than zero. The Autocorrelation is then computed as above. This estimate is equivalent to the estimate given in Heath et. al. 1983. While this estimator is asymptotically unbiased, care is necessary when studying its variance and statistical significance as the number of pairs at a given lag can vary.

Plots of the estimated autocorrelation function for each polynomial-detrended time series and each corresponding first-difference series are given in Figure 5.1. The autocorrelations of the polynomial detrended Si-II,

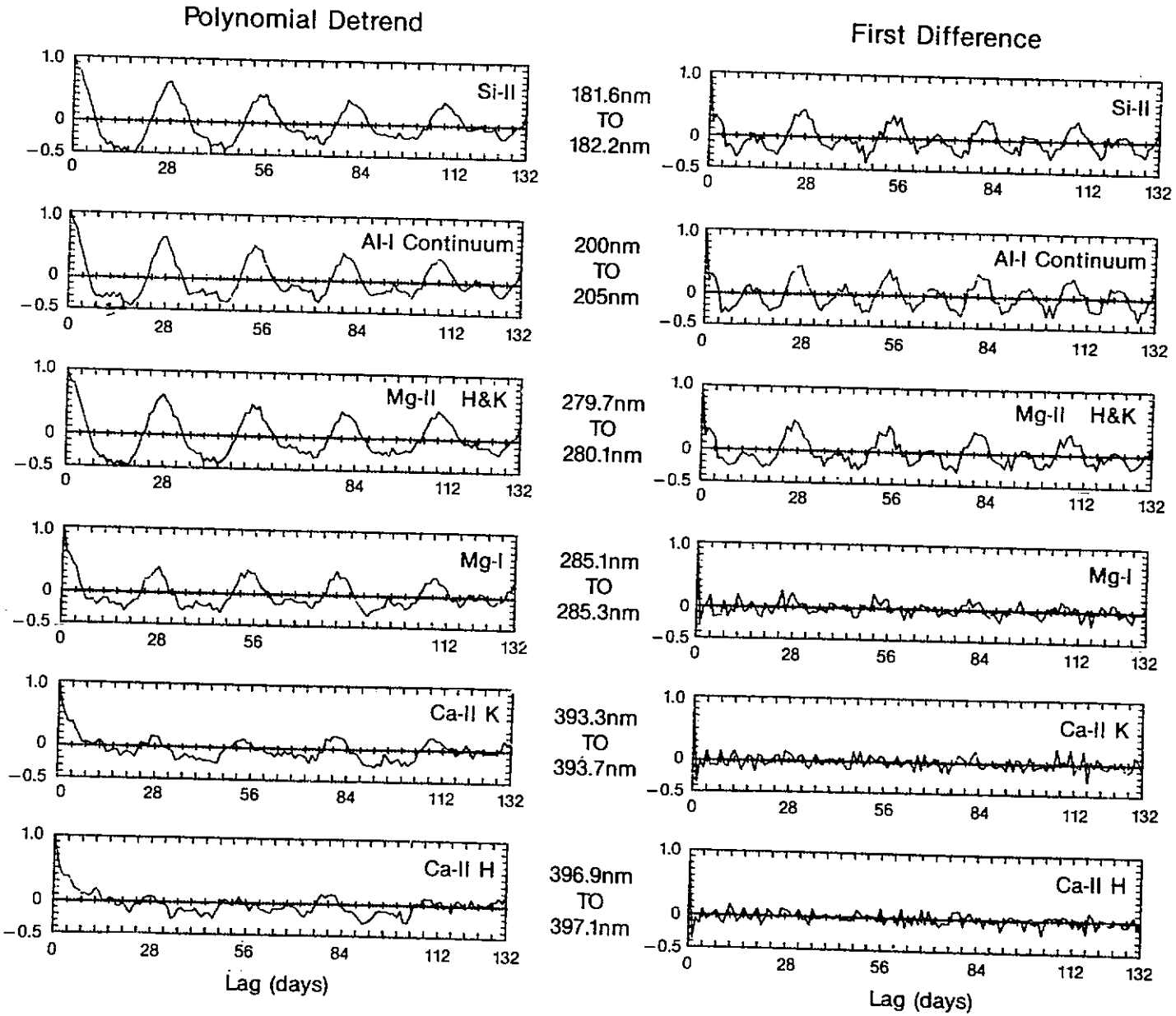
NIMBUS—7 Autocorrelation
Polynomial Detrend
First Difference
181.6nm TO 182.2nm
200nm TO 205nm
279.7nm TO 280.1nm
285.1nm TO 285.3nm
393.3nm TO 393.7nm
396.9nm TO 397.1nm
Si-II
Al-I Continuum
Mg-II H&K
Mg-I
Ca-II K
Ca-II H
1.0
0
−0.5
0
28
56
84
112
132
Lag (days)

Figure 5.1

Al-I continuum, Mg-II H&K, and Mg-I are all strongly oscillatory with a twenty-eight day period. These oscillations show dampening.

The Ca-II K and the Ca-II H series show weak but not statistically significant twenty-eight day oscillations. These two series show the correlation of neighbors dies after about five days.

The plots of the differenced data show a more detailed structure. Here the Si-II, Al-I continuum and Mg-II H&K series display both thirteen day and twenty- eight day oscillations. But the Mg-I, Ca-II K, and Ca-II H display no structure other than a weak negative correlation at lag one.

Periodic behavior in an autocorrelation function strongly suggest that solar processes represented by the Si-II, Al-I continuum, Mg-II H&K, and, to a lesser extent, the Mg-I line are related to events that occured about twenty eight and thirteen days earlier. The twenty-eight day period is about that of solar rotation and the thirteen day is about half a solar rotation.

The dampened oscillations suggests a class of time domain models called Seasonal ARIMA. Seasonal nonstationarity appears in the autocorrelation function as large and nearly equal values at the seasonal lag. At half the period there should be a large correlation of opposite sign. In the polynomial detrended data this does not happen. The out-of-phase correlations are flat suggesting the presence of another component. In the differenced series these areas show the presence of a thirteen-day component. To gain more information on the periodic structure of the series we turn to spectral analysis.

5.3 Frequency Domain Analysis

Spectral analysis views a time series as a complex wave pattern composed of weighted sinusoids. The method decomposes the observed time series into

frequency bands which contribute to the total variance of the series. The power spectrum provides information about the energy content of these frequency bands. If there are strong sinusoidal oscillations that contribute to the variability in an observed time series, a peak appears in the power spectrum at the corresponding frequency of each oscillation. In this way the power spectrum is used to identify the presence of multiple periodicities that may be hidden by other variations.

There are several different procedures used in spectral analysis. Among the more popular are periodogram analysis and power spectrum analysis. Both methods provide the same information about a given time series. However, both methods do produce a number of side effects which must be kept in mind when computing and interpreting a power spectra.

The first point to keep in mind is the actual width of the frequency bands. Band width directly ties in to the number of lags that are considered important in the autocorrelation function. This ties into a method called "lag-windowing" which we will discuss later in this section. The effect to be kept in mind at this point is that if you change the number of lags that are considered important you change: the band width, the number of frequencies in the discrete power spectrum, and the power of each frequency band.

Another effect to be kept in mind is the "aliasing effect". Aliasing tells us that the spectral density function of a continuous process sampled at discrete instants of time extends only over the frequency range $(-\pi/\Delta t, \pi/\Delta t)$ where Δt is sampling interval (one day in this case); and that the power at each point "w" within this frequency range is a superposition of the powers at the frequencies: w, $w \pm 2\pi/\Delta t$, $w \pm 4\pi/\Delta t$, ... The basic reason for this is that (t) is restricted to integer multiples of (Δt). As a result, we cannot distinguish between the frequency components exp(iwt) and

$\exp[i(w \pm 2k\pi/\Delta t)]$, $k = 1,2,3,\ldots$ The components in X(t) that have power at frequencies $w \pm 2k\pi/\Delta t$, $k=1,2,3,\ldots$, will appear to have power at frequency "w". These frequencies are said to be aliases of "w", and every frequency with non zero power outside the range $(-\pi/\Delta t, \pi/\Delta t)$ has an alias inside this range.

The aliasing effect in turn introduces another effect to be kept in mind. The power spectrum is defined over the range $(-\pi, \pi)$. But the frequency range we consider is finite because the process X(t) is sampled at discrete time intervals (Δt). The frequency $(\pi/\Delta t)$ is that frequency at which higher frequencies are "folded" down into the interval $(-\pi/\Delta t, \pi/\Delta t)$. This frequency is called the "Nyquist" or "folding" frequency, and it is the highest frequency about which we can get any information from a data set. Since the sampling interval is Δt, the sampling rate is $1/\Delta t$ observations per unit time. The angular frequency is given by $(\pi/\Delta t)$, and the equivalent frequency expressed in cycles per unit time is $f_N = (\pi/\Delta t)/(2\pi) = 1/(2\Delta t)$. Thus the highest frequency we can see is one half the sampling rate. For this analysis, the period of the Nyquist frequency is two days. Any variations with periods shorter than two days will fold into their corresponding alias of period greater than two days.

The usual model for a process with a purely discrete spectrum is given by the harmonic model:

$$X(t) = \sum_{i=1}^{K} A_i \mathrm{Cos}(w_i t + \phi_i) + e_t$$

where w_i are discrete frequencies on the range $(-\pi, \pi)$, A_i are the respective amplitudes, ϕ_i the respective phase, and K is the number of terms in the equation is to be determined. This equation may be rewritten in the form:

$$X(t) = \sum_{i=1}^{K} [A'_i \mathrm{Cos}(w_i t) + B'_i \mathrm{Sin}(w_i t)] + e_t$$

Periodogram and power spectrum analysis are search techniques that locate frequencies where periodicities occur. Even when these periodicities are hidden in the noise, the method will reveal their presence. Heuristically, the procedure underlying this analysis chooses a sufficiently fine set of frequencies $\{w_i \ (1 \leq i \leq N-1)\}$ and plots the squared amplitude $(A_i'^2 + B_i'^2)$ against w_i. If the w_i are sufficiently close to a frequency present in the time series, the squared amplitude will be nonzero. The normalized squared amplitude $\{(N/2)(A_i'^2 + B_i'^2)\}$ is ploted. The effect of the factor (N/2) being to magnify the difference between large and small amplitudes. The periodogram is defined as:

$$I_N(w) = (2/N) \left| \sum_{t=1}^{N} X_t \, e^{-iwt} \right|^2$$

where the frequencies are $w_i = (2\pi i)/N, \quad 0 \leq i \leq (N - 1)$. The periodogram is derived directly from the series X(t) via the Fourier transform.

Alternatively we may write the periodogram in the form:

$$I_N(w) = (2/N) \left[\sum_{t=1}^{N} X_t \, e^{-iwt} \right] \left[\sum_{r=1}^{N} X_r \, e^{-iwr} \right]$$

$$= (2/N) \sum_{t=1}^{N} \sum_{r=1}^{N} X_t X_r \, \mathrm{Cos}[(t - r)w]$$

The Sine terms vanish due to symmetry of the factor $(X_t X_r)$. Now let $s=(t - r)$, then (s) has the range $[-(N - 1)$ to $(N - 1)]$ for fixed (s), and (t) and (r) range from 1 to $(N - |s|)$. Substitution yields:

$$I_N(w) = (2) \sum_{s=-(N-1)}^{(N-1)} \left\{ (1/N) \sum_{t=1}^{(N-|s|)} X_t X_{t+|s|} \right\} \mathrm{Cos}[sw]$$

$$= 2 \sum_{s=-(N-1)}^{(N-1)} C^*(s) \, \mathrm{Cos}(sw)$$

where $C^*(s)$ is the biased sample autocovariance. The power spectrum is defined as:

$$P(f) = (1/\pi) \sum_{k=0}^{N-1} C(k)\, e^{(iwt)}$$

which is the Fourier transform of the unbiased autocovariance function. This is the relationship between the power spectrum and the periodogram.

This estimate of the spectral density function is not a statistically consistent estimate. The periodogram will display an erratic and wildly fluctuating form. The main reason for this is that the tail of the autocovariance function does not go to zero fast enough. The technique used to obtain a consistent estimator is to select a lag window that truncates the autocorrelation function by weighting the tail so that it smoothly approaches zero. The weighting function is called the spectral window or lag window, and the technique is called windowing.

The method for spectral estimation applied in this analysis computes the autocorrelation function following the procedure outlined in the last section for missing observations. A lag window one-fourth the number of days in the series (just over six solar rotations) is applied to the autocorrelation. A Tukey-Hanning window which is a cosine weighting function is applied to the function to reduce the effect of the tail. The Fourier transform is then taken. This combination was found to produce a satisfactory estimate of the spectral density. Figure 5.2 shows the results for both the polynomial detrended data and the first differenced data.

When the autocovariance function is used to estimate the power spectrum, the area under the curve represents the contribution to the total variance by the frequency band (w_i, w_{i+1}). Integrating the power spectrum over frequency

NIMBUS—7 Normalized Power Spectrum

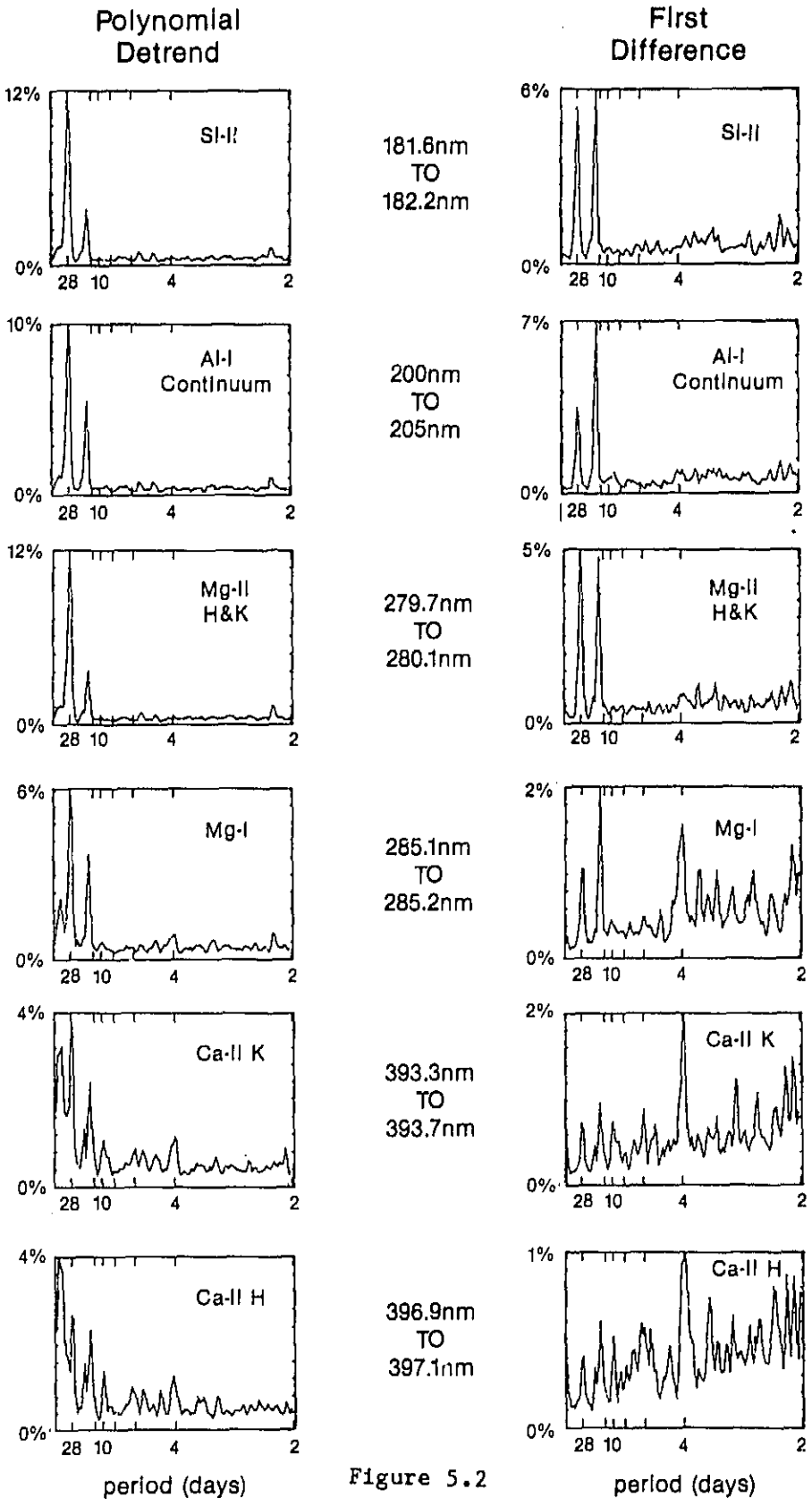

Figure 5.2

yields the total variance of the process. We used the autocorrelation function. This spectrum is called the normalized power spectrum. Integrating this spectrum over frequency produces unity. It represents the percent contribution to the total variance by frequency band (w_i, w_{i+1}).

The NIMBUS-7 data discussed in the last section show strong cyclical behavior around twenty-eight days. At thirteen days the oscillation appears confused. The power spectra for polynomial detrended data show a strong peak at twenty-eight days with a secondary peak at thirteen days in all the lines. The peaks for the Ca-II K and Ca-II H lines are weaker and a low frequency component is present. Also seen in these two lines are small multiple peaks that are due to spikes that remain in the data.

The differenced data also show two dominant peaks. The Si-II, Al-I continuum, and Mg-II H&K lines show a dominating thirteen-day oscillation and a strong twenty-eight day oscillation. A four-day component dominates the Mg-I, Ca-II K, and Ca-II H lines but there still remain thirteen-day and twenty-eight day peaks. We interpret the four-day component (the second fourth-day problem) to be due to an instrumentation problem while the thirteen and twenty-eight day periods are due to solar activity.

Also seen in these three spectra is a tendency for the power to increase with frequency, and a large multiplicity of peaks. Differencing a time series weights the power in proportion to its corresponding frequency. In addition, a random component composed by numerous spikes and noise events is enhanced by differencing. As noted earlier, spikes introduce spurious peaks into the spectrum. In addition, differencing of data sets that contain missing observations change the frequency structure because the time interval between successive observations is not constant. New frequencies may be introduced. Also, frequencies higher than the Nyquist frequency may be created and folded

down into the frequency range of the power spectra. There is no way that the effect of differencing a series with non-constant sampling interval can be traced into the frequency domain. These results show that where there are missing data, the method of differencing should not be used in spectral analysis.

The thirteen and twenty-eight day peaks are well defined in both the polynomial detrended data and the differenced data. But the magnitude of the thirteen day peak is different, being consistently smaller for the detrended data. This may result from the polynomial not removing all the long term variation; or differencing may decrease the amplitude of long-term variations relative to short term variations and create components that are not real. As a result, spectra based on differenced data should be considered suspect, and should not be used for interpretation. Because the peaks are narrow and well defined, we may conclude that there is a periodic structure in the NIMBUS-7 data. This structure is very weak in processes characterized by the Ca-II H and Ca-II K lines.

Examination of time series plots shows that the amplitude is not constant and that the phase drifts. The result is nonstationarity in the variance. Physical interpretation of the spectrum for nonstationary processes is essentially the same as for stationary processes. The difference though is that we can no longer represent X_t as the sum of sines and cosines. This aspect will be addressed in detail in chapter seven.

6. BIVARIATE ANALYSIS

This preliminary analysis is extended to more than one variable. Multivariate time-series analysis provides a number of methodologies for analysis of complex phenomena that involve primary as well as auxiliary variables that extend across time.

Bivariate analysis is the most primitive level of multiple time-series analysis. It describes the fluctuations of a system of two variables over time by searching for concomitant variation. In time-domain analysis, the cross correlation function characterizes how two time series correlate with one another. It provides information on lead/lag relationships among the variables. In frequency-domain analysis, the bivariate cross spectrum provides information about coherent sinusoidal structures in the two time series and their phase relationships.

Techniques exist for analysis of more than two variables (Box and Tiao; 1977), (Akaike; 1979). These methods are called 'State Space Techniques'. The methods remain in development and are not set up to handle missing observations. The advantage of these techniques is evident from the fact that bivariate analysis of six variables requires fifteen separate analyses be performed. These state space techniques reduces this to one single analysis. Because the NIMBUS-7 are redundant, we present only two bivariate analysies.

6.1 Cross Correlation Analysis

Bivariate analysis can be applied to two types of situations (Jenkins and Watts, 1968). In the first, two time series arise on an equal footing and we are interested in the correlation between them. In the second, and more interesting situation, two time series are causally related and one series is regarded as an input to a process while the other is regarded as

the output. A model, called the transfer function, is constructed that mathematical represents how the process modifies the input to produce the output. For this analysis we will deal with the first situation.

Following the notation of the last chapter, suppose we have two time series X(t) and Y(t). To describe this bivariate process it is useful to know the moments up to the second order. In univariate processes, the moments up to second order are the mean and the autocovariance function. For a bivariate process, the moments up to second order consist of the mean and autocovariance function for both time series plus a new function, called the cross-covariance function:

$$\text{Cov}[X(t),Y(t+k)] = \begin{cases} (1/N) \sum_{t=1}^{N-k} X(t)Y(t+k) & k = 0, 1, 2, \ldots, (N-1) \\ (1/N) \sum_{t=1-k}^{N} X(t)Y(t+k) & k = -1, -2, \ldots, -(N-1) \end{cases}$$

for purposes of notation, let:

$$C_{xy}(k) = \text{Cov}[X(t),Y(t+k)]$$

Note that $C_{xx}(k)$ is simply the autocorrelation and it is symetric with respect to plus or minus the lag. Unlike the autocovariance function, the cross-covariance function is not an even function. That is, for the autocovariance function:

$$C_{xx}(k) = C(k) = C(-k) = C_{xx}(-k)$$

where k is the lag time. For the cross-covariance function this condition does not hold; namely, $C_{xy} \neq C_{yx}$. Instead we have the relationship:

$$C_{xy}(k) = C_{yx}(-k)$$

where the two subscripts are reversed. As with the autocovariance function, we standardize the cross covariance to obtain the cross-correlation function, which is defined as:

$$R_{xy} = C_{xy}(k)/[C_{xx}(0)C_{yy}(0)]^{.5}$$

This function measures the correlation between X(t) and Y(t + k). Whereas the autocorrelation at lag zero is equal to one, the cross-correlation function may not be. Also, the cross correlation structure is not necessarily symetric about lag zero. These facts are often overlooked by analysts.

We make all the assumptions about stationarity as were made in the last chapter. In addition, we now assume the two processes to be covariance stationary, which means the covariance doesn't change with time. Again we assume there are data missing from both series.

The cross-correlation function is estimated in the same way as the autocorrelation function. Now however, the indicator function for missing data are for the two different series. This is also an asymptotically unbiased estimate of the cross-correlation but because the variance of the estimator depends on the number of observations, care must be used in determining the significance of the estimate.

Even though the estimators are asymptotically unbiased and consistent, succesive estimates are not independent. They are themselves autocorrelated. In addition, the variance of the estimators depend on the autocovariance in the two time series. Two time series, which are actually uncorrelated can give rise to spurious correlations. Thus if a test is required for non-zero correlation, the series should first be pre-whitened by differencing. This is achieved by first ARIMA modeling the two time series separately and removing the autocorrelation structure. No standard techniques presently are available to do this. Keep this in mind as we examine the cross-correlation below.

Figure 6.1 shows the cross-correlations for Mg-I verses Mg-II H&K lines and the Si-II verses Mg-II H&k lines. For both, the correlation structures

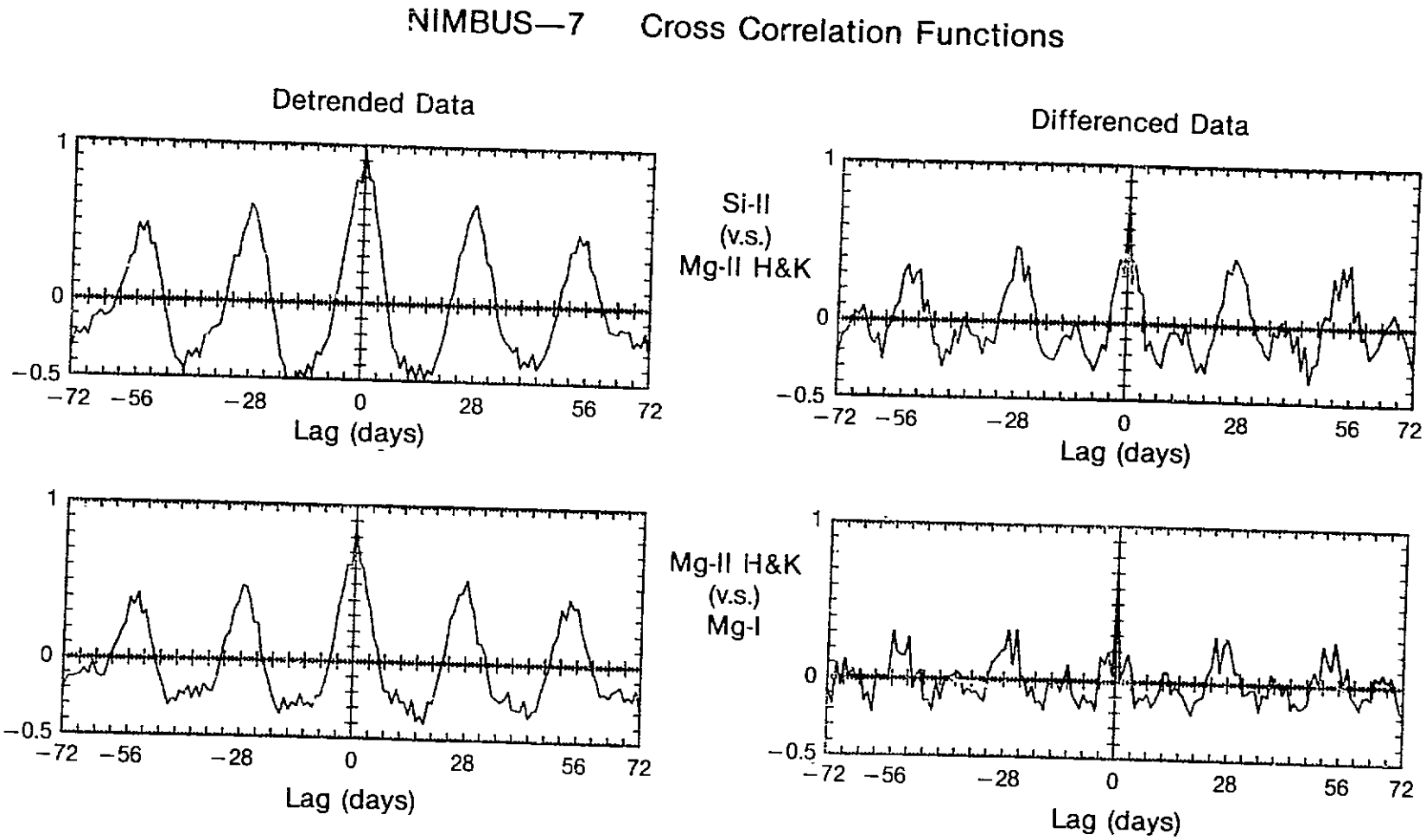
NIMBUS—7 Cross Correlation Functions
Detrended Data
Differenced Data
Si-II
(v.s.)
Mg-II H&K
Mg-II H&K
(v.s.)
Mg-I
1
0
−0.5
−72 −56 −28 0 28 56 72
Lag (days)

Figure 6.1

are more or less symmetric. For the polynomial detrended data the Si-II and Mg-II H&K data are almost exactly the same. Remember, the autocorrelation function for these two series is almost identical. Very strong periodic structures are seen in both cross-correlation functions. The differenced time series also show a correlation structure. The zero lag correlation is over 0.8 for both. Strong oscillatory behavior is also present.

Again, the autocorrelation structures are very similar for all three of these series. What we are seeing here is the concomitent variation due to similar time structures in each of the three series. The cross-correlation function is telling us they are very similar in time structure. But remember, concomitant variation does not necessarily imply causation. The determination of causation remains in the hands of science. One way of studying this concomitant variation is by the use of trasfer functions. A transfer function is a linear equation which relates the past of one time series to the present or future of another time series. As of yet though, there are no methods for time series that contain missing data.

6.2 Cross Spectrum Analysis

The cross-correlation function is a natural tool for examining the relationship between two time series in the time domain. In this section we apply analysis in the frequency domain. Analogous to the power spectrum, the cross spectrum of a bivariate process is the Fourier transform of the cross covariance function. But because the cross correlation function is not an even function of lag, the cross spectrum is a complex function.

The real part of the cross spectrum is called the co-spectrum:

$$Co(w) = (1/\pi) \sum C_{xy}(k) \cos(wk)$$

The complex part of the cross spectrum is (with a minus sign):

$$Qu(w) = (1/\pi) \sum C_{xy}(k) \sin(wk)$$

so that:

$$P_{xy}(w) = Co(w) - iQu(w)$$

is the definition of the cross-spectrum. The cross spectrum expresses the covariance accounted for by oscillations at frequency (w) common to both series. Alternatively, The cross spectrum can be expressed in the form:

$$P_{xy}(w) = A(w)e^{[i\phi(w)]}$$

Where A(w) is the cross amplitude spectrum:

$$A(w) = [Co^2(w) + Qu^2(w)]^{.5}$$

and $\phi(w)$ is the phase spectrum:

$$\phi(w) = \tan^{-1}[-Qu(w)/Co(w)]$$

A more useful function than the cross amplitude spectrum is the squared coherency spectrum:

$$Ch(w) = A^2(w)/[P_x(w)\ P_y(w)]$$

where each term in the denominator is the respective power spectrum.

The CO, QUAD, Phase and Coherence are redundant functions in that any two completly define the cross spectrum. Normally, one needs to examine three plots to understand the relatioship between two series. The coherence is perhaps the most useful. It is a measure of the correlation between two series at each frequency and is analogus to the square of the correlation coefficient in linear regression. It takes on values between zero and one. Even if the two series have related signals obscured in noise, in which case the cross correlation function may not be sensitive to a relationship, the coherence will extract the relationship.

If there is a strong coherence, but the series are phase shifted or tend to have different envolope structures, the phase spectrum will show a structure. Note however, the coherence must be strong for the phase to have much meaning. Otherwise, the phase may fluctuate wildly.

A third spectrum, the Co spectrum is useful in interpretation because it represents the covariance between coefficients of the in-phase components in the two processes; and unlike the quadrature, it is a real number. The quadrature spectrum represents the covariance between coefficients of the out-of-phase components in the two series.

Figure 6.2 shows the Co-spectrum, Phase spectrum, and Coherency spectrum for the polynomial-detrended data. Notice the strong similarity between the Co-spectrum and the two corresponding power spectra. The dominant source of covariance between in-phase components in all NIMBUS-7 data are the twenty-eight and thirteen day oscillations. Notice the strong coherence between Si-II and Mg-II H&K at almost all frequencies. Corresponding to this coherence is an almost zero phase spectrum. Note the coherence between Mg-II H&K and MG-I is not as strong. However, the thirteen and twenty-eight day events are still strongly coherent. The phase spectrum shows that as coherency drops, phase begins to change. This is expected. But in the region about twenty eight days, there is a U-shape in the phase. The negative slope means that there is a slight tendency for the Mg-II twenty-eight day event to lead the MG-I event, while the positive slope implies a tendency to follow the Mg-I event. However, both the magnitude of the phase change and the number of twenty-eight day oscillations are small. This change is not statistically significant.

Figure 6.3 shows the three spectra for the differenced series. Again, the co-spectrum is very similar to the power spectrum. The thirteen day

Polynomial Detrended Data

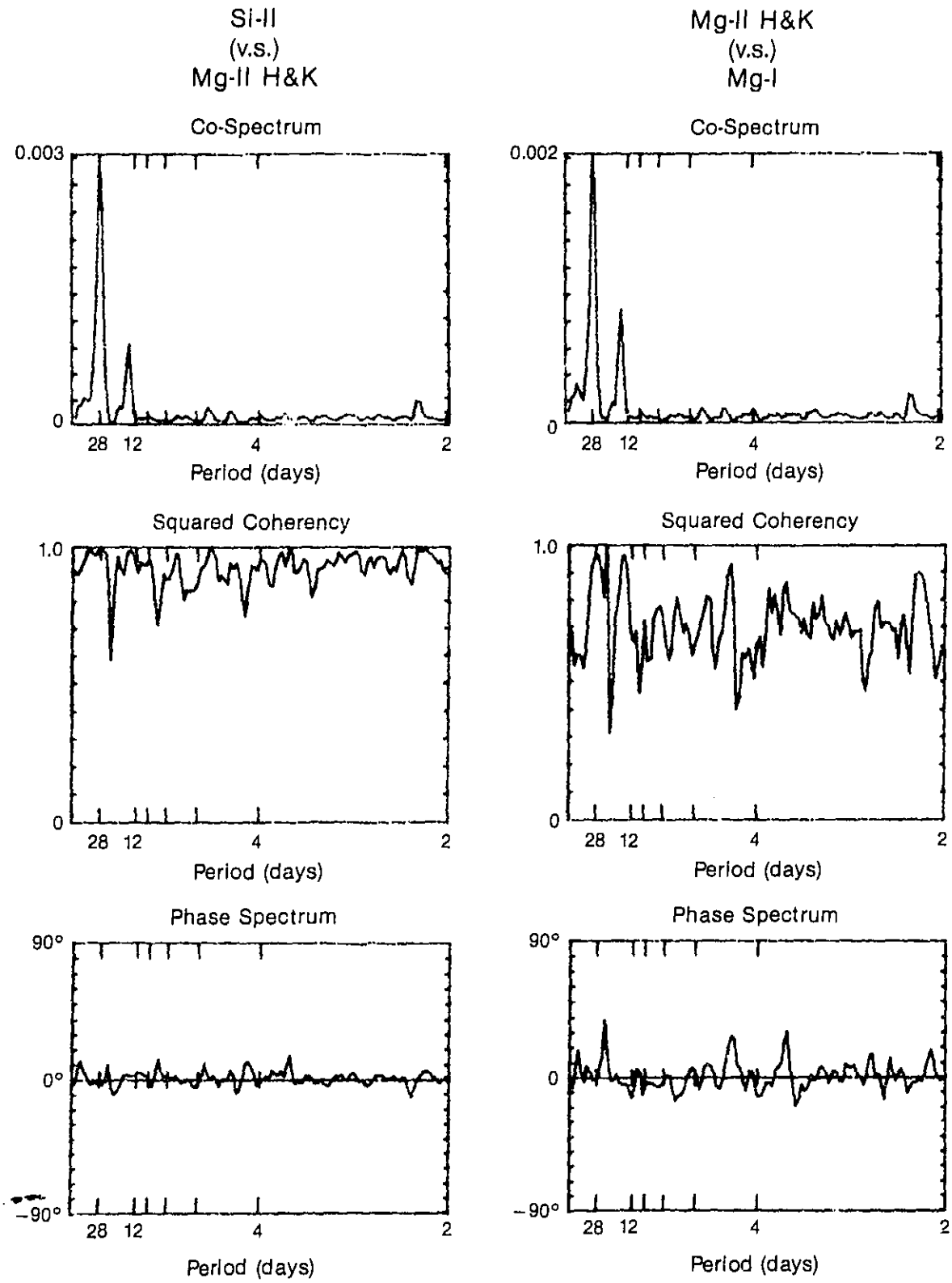

Figure 6.2

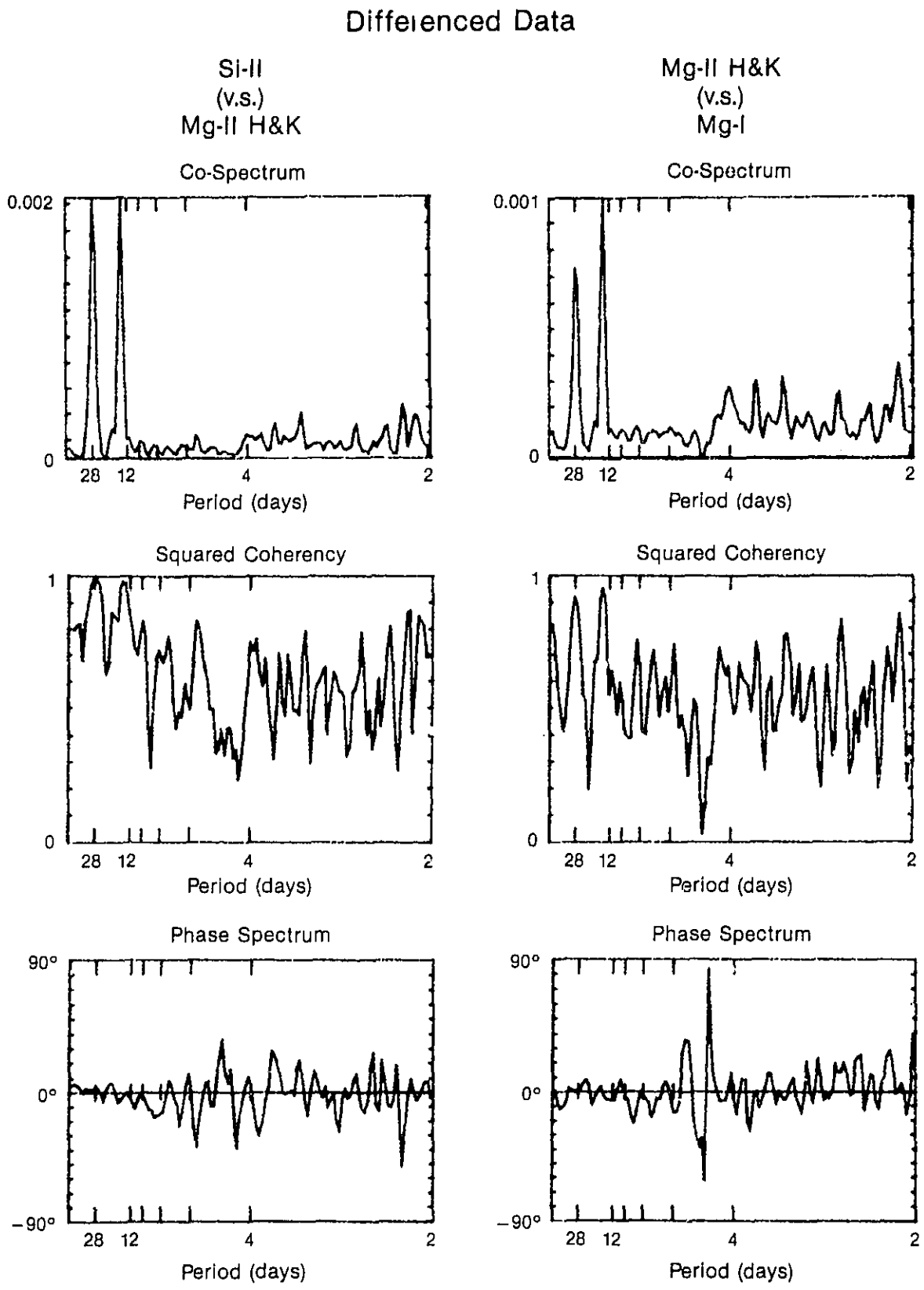
Differenced Data
Si-II
(v.s.)
Mg-II H&K
Mg-II H&K
(v.s.)
Mg-I
Co-Spectrum
0.002
0
28 12 4 2
Period (days)
Co-Spectrum
0.001
0
28 12 4 2
Period (days)
Squared Coherency
1
0
28 12 4 2
Period (days)
Squared Coherency
1
0
28 12 4 2
Period (days)
Phase Spectrum
90°
0°
−90°
28 12 4 2
Period (days)
Phase Spectrum
90°
0°
−90°
28 12 4 2
Period (days)

Figure 6.3

spike is more dominant in these series. But the phase and coherence structure is about the same as the polynomial detrended data. Again, as we noted in the last chapter, the frequency structure of the differenced data is suspect because of the random missing data structure. The differenced data should not be used for analysis. These results are presented only for their instructive nature.

In all, the frequency and time structues of the data considered in this report are very similar. The only difference being in the Ca-k and Ca-H time series which are noisier. Yet the thirteen-day and twenty-eight day variations are still present, coherent, and approximately in-phase across the spectrum. Because of these concomitant autoregressive structures and the twenty-eight and thirteen-day seasonal structures, no inference concerning the interrelationships between the time series can be made at this time. Future analysis using ARIMA modeling is called for.

7. COMPLEX DEMODULATION ANALYSIS

In chapter five, spectral analysis indicated the presence of two periodic components: a thirteen-day variation and a twenty-eight day variation. The twenty-eight day component is due to active regions being born, developing, and dying on one side of the sun, and the roughly twenty-eight day solar rotation. The thirteen day component results when active regions are on opposite sides of the sun.

A typical harmonic model for such a process is:

$$X_t = Ae^{i(2\pi/28)t} + Be^{i(2\pi/13)t} + Z_t$$

where:
- A denotes the amplitude of the 28-day component.
- B denotes the amplitude of the 13-day component.
- Z_t denotes the noise process.
- t denotes the day.
- i indicates an imaginary number.
- X_t denotes the observed value.

This is a simple representation of the data in terms of Sine and Cosine terms with constant amplitude and phase (i.e. amplitude and phase are invariant over time).

But the NIMBUS-7 data present a situation where amplitude and phase drift over time. We observe in figure (4.4) that both the 13-day and 28-day oscillations intermittently grow and fade over time. In the absence of such consistent structure, we cannot immediately talk about power distributions over frequency as we did in chapter 5. A nonstationary process cannot be represented as the sum of sine and cosine terms. Instead, we have to represent it as a sum of other kinds of functions.

This requires a more generalized concept of frequency. For example, the autocorrelation for the Si-II line has the form of a damped sine wave, say,

$$R(k) = A\, e^{(-t\ /a\ )}\ \cos(w_o t + \phi)$$

If we carry out the conventional Fourier analysis on this function there will

be power at all frequencies. The shape of the peak consists of two Gaussian functions, one centered at w_o and the other at $-w_o$. The width of the peak will be inversly proportional to the parameter (a). In other words, to reproduce R(k) in terms of sine and cosine functions, we must include all frequencies. However, we can just as well say that R(k) has just two frequency components ($w=w_o$ and $w=-w_o$), each component having a time varying amplitude described by the exponential function above.

By frequency we now mean the function R(k) can be described loosely as having an oscillatory form, and the Fourier transform concentrates power around w_o. Thus if we have a non-periodic function X(t) whose Fourier transform has an absolute maximum at frequency w_o, we define w_o as the frequency of this function. The arguement is that X(t) behaves locally like a sine wave with frequency w_o, modulated by a smoothly varying amplitude function. More generally, the sine wave may be modulated by a slowly varying phase function, amplitude function, or both. This is the type of reasoning presented by Priestly (1981) in his chapter on evolutionary spectra, and Chatfield in his chapter on complex demodulation.

With this in mind, the simple model above is now rewritten in a more generalized form:

$$X(t) = A[1 + a_1(t)]e^{i[(2\pi/28) + \phi_1(t)]} + B[1 + a_2(t)]e^{i[(2\pi/13) + \phi_2(t)]}$$

where A and B are constant amplitudes for the twenty-eight and thirteen day variations, a_1 and a_2 are functions modulating the respective amplitudes, and ϕ_1 and ϕ_2 are functions modulating the respective phases. In fact, to be general, these modulation functions do not need to be deterministic. They can be generated from stochastic (random) functions. An example of such processes are Markov Chains.

Complex demodulation is a version of harmonic analysis. It seeks to describe the form of the amplitude and phase of an oscillation. It is local in that the amplitude and phase are determined only by the data in the neighborhood of an observation at time (t), not the whole series. The method seperates various signals that are simultaneously present but at different frequencies by assuming a particular signal is modulating the observed series. Separation is then accomplised by separation of carriers that were identified through spectral analysis.

For this analysis we examine only the Al-I continuum. The time series were demodulated at both a period of twenty-eight days and thirteen days. Figure 7.1 shows the amplitude and phase plots. The amplitude plots show there is indeed substantial variation in both the thirteen-day variations and twenty-eight day variations. But, the amplitudes are out of phase. When the twenty-eight day variations are large, which is more in the second year, the thirteen-day variations are small. Just the opposite variation is seen in the thirteen-day amplitude. The largest twenty-eight variations are about 1.5 times larger than the largest thirteen day variations.

The phase plots also show an interesting structure. When the phase for the twenty-eight day oscillations lock into a more or less linear pattern, the thirteen-day phase angle varies wildly. As with the amplitude, just the opposite occurs when the thirteen day phase locks into a pattern. This result suggests different processes dominate the thirteen-day periodicities than those that dominate the twenty-eight periods. This would not be expected if the thirteen day periodicities were primararily a harmonic of the twenty-eight day periods. The sun does appear to be experiencing different episodes of behavior throughout this two year period.

Note that in any time interval in which the phase is a linear function

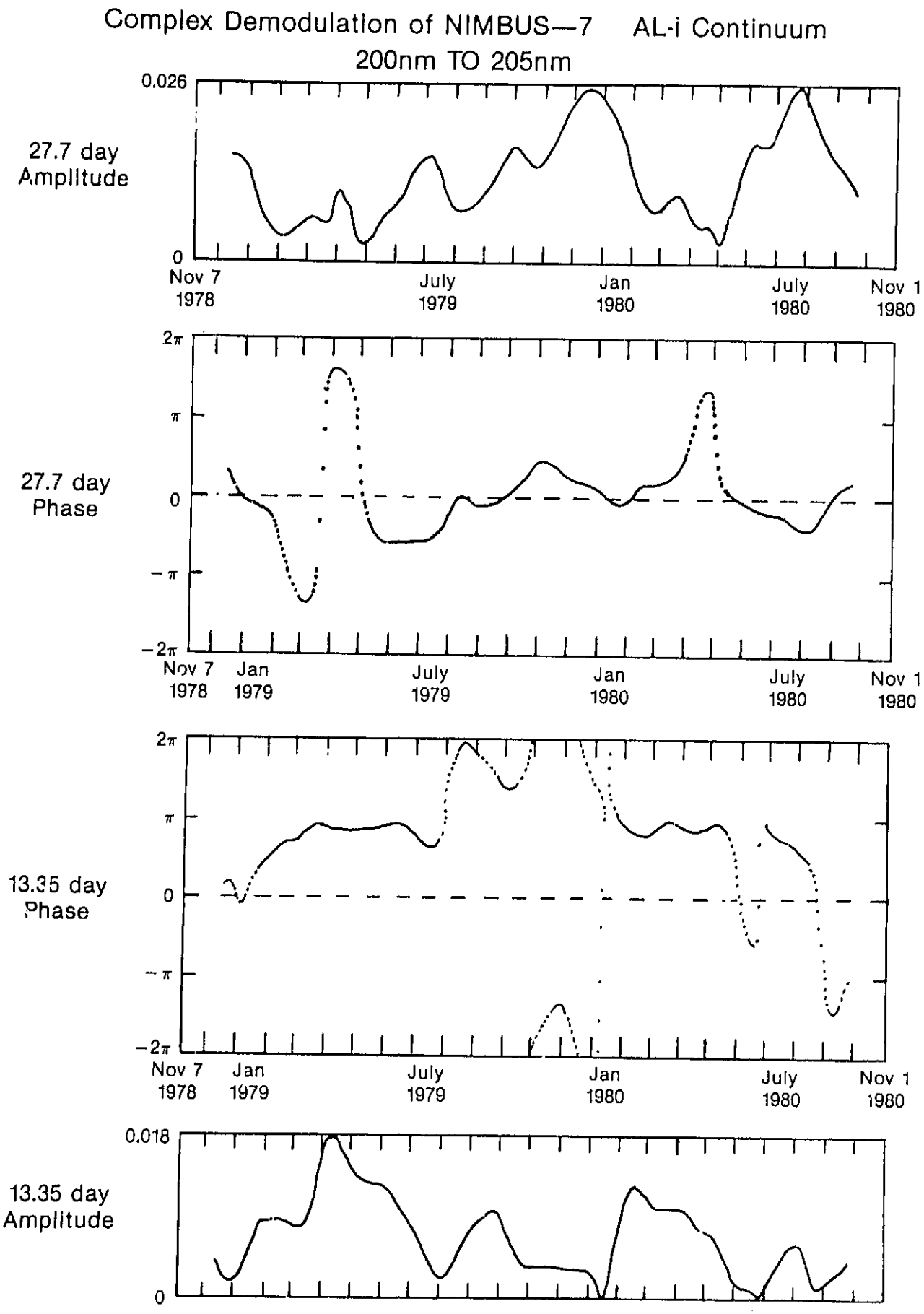
Complex Demodulation of NIMBUS—7 AL-i Continuum
200nm TO 205nm
27.7 day Amplitude
0.026
0
Nov 7 1978
July 1979
Jan 1980
July 1980
Nov 1 1980
27.7 day Phase
2π
π
0
−π
−2π
Nov 7 1978
Jan 1979
July 1979
Jan 1980
July 1980
Nov 1 1980
13.35 day Phase
2π
π
0
−π
−2π
Nov 7 1978
Jan 1979
July 1979
Jan 1980
July 1980
Nov 1 1980
13.35 day Amplitude
0.018
0

Figure 7.1

(a + bt) the oscilations are generated by:

$$A[1 + a_1(t)]\cos[ft + (a + bt)] = A[1 + a_1(t)]\cos[(f + b)t + a]$$

This is a modulated sinusoid of frequency (f + b) phase shifted by (a). The twenty-eight day variations show negative slope for the first three months of data suggesting a more rapid rotation in this period. An overall linear increase begining on May 15, 1979 and ending in April 1980, suggests an overall slowing in rotation for this period. But during this period there are a number of slope changes suggesting the twenty-eight day rotation speeds up and slows down. Beginning in June 1984, we see a speed up followed by a slowing at the very end. Clearly, when the twenty-eight day rotations are dominant, their period varies in time.

The thirteen-day variations display more constant variation when their amplitudes are dominant. This suggests a more or less constant rotation structure associated with the thirteen day frequency, but phase shifted. Three episodes are seen in the thirteen day phase plot. The episodes of February, 1979 to June, 1979 and February, 1980 to mid May, 1980 display almost constant slope. The brief episode of July, 1980 to mid August, 1980 shows the thirteen-day rotation are faster.

Harvey (1983) has noted similar episode structures in his 1083nm Helium data. He only studies the twenty-eight day rotations. If we consider only the period of May 15, 1979 to April, 1980, there occur four episodes of variation in the amplitude plot: June through July, 1979; August through October, 1979; a major episode November, 1979 through February, 1980; and a minor episode of February through March, 1980. Note that the phase for each of these episodes is different. Harvey suggests that this this result occurs because each complex associateded with an episode is unique. But we can further note that the first and last episodes in this sequence overlap

episodes of thirteen day events.

Bouwer (1984) used Anharmonic Frequency Analysis to determine the episode structure for this two year period at 180 nm. His first two epoch boundaries (6, Mar, 79 and 30, July, 79) bracket a thirteen day episode. The remaining boundaries (23, Nov., 79; 17 Mar., 80; and 24, July, 80) do not corresond well to any structure in the amplitude or phase structures.

As was shown above, the method can also be applied to the autocorrelation function to determine the form of decay of the sinusoidal behavior. This result will be useful in determining the form of relationship between solar rotations, and initially estimating the form of the ARIMA model.

8. FUTURE ANALYSES

The analyses presented in this manuscript are based on only two years of data. We know that there are twenty-eight day oscillations and thirteen-day oscillations. There also appears a random structure which may or may not be solar in origin. Complex demodulation has shown that these two rotational processes vary oppositely in amplitude and phase over this two year period. However, there is insufficient data to determine if there is any long-term pattern to this nonstationary character. Future analysis of rotational modulation must wait until longer time series are available.

ARIMA modeling techniques do not as yet exist for data sets with missing data. These techniques work best for short time series. There are few papers that explain how such procedures can be developed. Seasonal ARIMA modeling seems to hold the key for further insight into solar variability and forecasting. In fact, it is essential for any future multivariate analysis investigating linkage structures between Earth climate variability and solar variability. In the next year techniques will be developed that allow both univariate ARIMA modeling of missing data and bi-variate ARIMA modeling of multiple time series that contain missing observations. This development will assist not only climate modeling but comparison of data bases and comparison of other solar indices as well.

In addition, four day medians can be computed using the NIMBUS-7 data. This will give a data set that has no missing data and as the median is not susceptible to spikes, will reduce the noise. Standard multivariate ARIMA techniques can be applied to these series. Their results should be consistent with methods developed for series with missing data. By using a sampling interval of four days, we obtain a folding frequency of eight days. This will allow an investigation into the relationship between thirteen-day

variations and twenty-eight day variations.

New methods for handling of the diffuser degradation problem will also be developed. This will allow the ARIMA methods to be accurately applied in forecasting long-term solar variability.

9. CONCLUSIONS

The second year (Nov. 1979 - Nov. 1980) of NIMBUS-7 observations contains larger 28-day variations than during the first year. Strong 28-day variations due to an inhomogeneous distribution of solar active-region plages with solar longitude coupled with 28-day solar rotation dominated the second year through January, 1980, and from late May to October, 1980. A strong 13-day period was present from February through May, 1980, which was caused by two concentrations of strong plages located nearly 180^{o} apart in solar longitude. This case of strong 13-day periodicity together with the case from late January to early June in 1979 during the first year of observations means that 13-day periodicity dominated the NIMBUS-7 data for about one third of the time during the first two years of measurements. See Figure 2.1.

The main spectral features in the percent variation as a function of wavelength for individual short-term variatons are the solar Al I absorption edge just below 210 nm, the strong enhancement in the Al I continuum below 207 nm, the strong enhancement of the Mg II H & K lines at 280 nm, and a moderate enhancement in the 210 - 263 nm range of a combination of Al I, Si I and Fe I & II lines and possibly a Mg I continuum. See Figures 2.2 - 2.9. The 180 - 210 nm band is very important for photodissociating stratospheric O_2, which leads to the production of ozone. The 210 - 290 nm band is important for heating the stratosphere and the photodissociation of ozone. The 195 - 225 nm "window" range is important because it penetrates deep into the stratosphere. To first order, the spectral shape of these short-term variations is fairly constant. Short-term enhancements of the Al I continuum are highly correlated with those in the 212 - 241 nm wavelength band, where the latter includes the Mg I continuum and numerous lines of Al I and Fe I. See Figure 3.4. A second order effect occurs where the Al I enhancement is larger if the wavelength slope of the Al I continuum enhancement is large.

Techniques for removing noise and long-term trends from the NIMBUS-7 data have been developed. These same techniques will be applied to the third and fourth year of observations and will be used in numerous studies comparing the NIMBUS-7 solar UV data with other solar radiation measurements and indices of solar activity.

Time domain analyses showed a strong peak in autocorrelation at about 28 days and integer multiples of 28 days in the Mg I line at 285 nm and at shorter wavelengths, with corresponding weak and noisy peaks in the Ca H & K lines. See Figure 5.1. The NIMBUS-7 SBUV passband of about 1 nm is much wider than the width of these narrow Ca lines and the observations are sensitive to noise from any small jitter in the wavelength steps of the monochrometer. The autocorrelation function for the polynomial detrended data showed only weak evidence for a 13-day periodicity through the lack of a deep negative peak near 13 days. The autocorrelation for the first-difference data shows peaks at about 13 days and integer multiples of 13 days in the Mg II lines at 280 nm and at shorter wavelengths. The first-difference technique weights the periodicities in proportion to their frequency, thereby reducing the relative strength of the 28-day period and enhancing the 13-day period. On the otherhand, it greatly enhances the high-frequency noise in the narrow Mg I and Ca H & K lines causing the autocorrelation for the first-difference data for these lines to be essentially noise.

The power spectrum analysis similarly showed major peaks near 13 and 28 days. See Figure 5.2. In the broad Mg II lines at 280 nm and at shorter wavelengths, there are no other strong spectral features. In the narrow Mg I and Ca H & K lines, there are many other lines with periods less than 13 days, the strongest being 4 days, which dominates the Ca H & K lines for the first-difference data. We do not attribute this four-day periodicity to the four-

day noise discussed in section 4.1 or to the fact the edited data are missing every four days. There is no important four-day peak for the Mg II and Si II lines or Al I continuum in figure 5.2. The main fourth-day problem was successfully removed. We suggest that the peak at four days in Figure 5.2 for the narrow Mg I and Ca H & K lines (narrow relative to the SBUV 1 nm passband) is caused by a second type of instrumental four-day problem, namely that the wavelength steps are slightly off on one of the remaining three out of four days of data, which affects narrow solar UV spectral features much more than broad UV features. Our studies of SBUV wavelength jitter show that it is only a fraction of one wavelength step, i. e. a fraction of 0.2 nm.

Note that the ratio of the 13-day peak to the 28-day peak in Figure 5.2 is larger for the Mg I line and the Al I continuum than for the Mg II and Si II lines. The Mg II and Si II lines originate from somewhat higher altitudes in the solar atmosphere than the Mg I and Al I emissions. This difference in 13-day periodicity may be caused by a broader CMD dependence of plage emission for the Mg II and Si II lines than for Al I continuum and the Mg I line.

The cross correlation and co-spectrum analyses showed that the UV variations are highly correlated and in phase, including the 28-day and 13-day variations. The complex-demodulation analysis showed that **the 13-day spectral peak is not simply a harmonic of the 28-day peak.** There are certain times when the 28-day periodicity is strong. During these episodes, any related 13-day harmonic is weak. At other times, the 13-day periodicity dominates and during these episodes the 28-day component is weak relative to the other episodes when the 28-day periodicity dominates. Studies of the Ca-K plages during the 13-day episodes simply show two groups of strong plages (in excess over the amount of plage present during a local temporal minimum) located about 180^{o} apart in solar longitude while there is only one main group of

plages during the 28-day periodicities. For the first two years of NIMBUS-7 observations, the complex demodulation analysis gives our best estimate for the period of the 28-day variation being 27.7 days, and for the 13-day variation being 13.4 days.

10. ACKNOWLEDGEMENTS

We thank Wanda Busby of NOAA for her aid in data processing, Dr. Judith Lean of CIRES for helpful discussion, and Dr. Hongwoo Park and his associates at Systems & Applied Sciences Corporation in Riverdale, Maryland, for preparation of the data tapes used in our analyses.

11. REFERENCES

Akaike, H., TIMSAC-78, Computer Science Monographs, 11, Inst. Stat. Math, Toyoko.

Bloomfield, P., Fourier Analysis of Time Series: An Introduction, John Wiley and Sons, 1976.

Box, G. P., Jenkins, G. M., Time Series Analysis, Holden Day, 1976.

Box, G. E., Tiao, G. C., A Canonical Analysis of Multiple Time Series, Biometrika, 355 - 364, 1977.

Chatfield, C., The Analysis of Time Series: An Introduction, Chapman and Hall, 1982.

Donnelly, R. F., D. F. Heath and J. L. Lean, Active-region evolution and solar rotation variations in solar UV irradiance, total solar irradiance, and soft X rays, J. Geophys. Res., 87, 10318 - 10324, 1982.

Hald, A., Statistical Theory With Engineering Applications, John Wiley, 1952.

Heath, D. F., A. J. Krueger, H. A. Roeder and B. D. Henderson, The solar backscatter ultraviolet and total ozone mapping spectrometer (SBUV/TOMS) for NIMBUS G, Optical Eng., 14, 323 - 331, 1975.

Heath, D. F., A review of observational evidence for short and long term ultraviolet flux variability of the sun, Sun and Climate, Centre National D'Etudes Spatiales, 18 Avenue Edouard - Belin, 31055 Toulouse Cedex, France, 447 - 471, 1980.

Heath, D. F., R. F. Donnelly and R. G. Merrill, NIMBUS-7 SBUV Observations of Solar UV Spectral Irradiance Variations Caused by Solar Rotation and Active-Region Evolution for the Period November 7, 1978 - October 26, 1979, NOAA Tech. Rept. ERL 424-ARL 7, Air Resources Lab., NOAA ERL, Boulder, Colorado 80303, 45 pp., 1983.

Heath, D. F., Space observations of the variability of solar irradiance in the near and far ultraviolet, J. Geophys. Res., 78, 2779 - 92, 1973.

Jenkins, G. M., Watts, D. G., Spectral Analysis and Its Applications, olden Day, 1968.

Jones, H. J., Spectrum Estimation With Missing Data, Ann. Math. Statist., 23, 387-398, 1971.

Kendall, M. G., Stuart, A., The Advanced Theory of Statistics, Vol. 3, Griffin, London, 1966.

Lean, J. L., O. R. White, W. C. Livingston, D. F. Heath, R. F. Donnelly, and A. Skumanich, A three-component model of the variability of the solar ultraviolet flux: 145-200 nM, J. Geophys. Res., 87, 10307 - 10317, 1982.

Priestly, M. B., Spectral Analysis and Time Series, Vol. 1 and 2, Academic Press, 1981.